12-2017

Influence of Beam Rotation on the Response of Cantilevered Flow Energy Harvesters Exploiting the Galloping Instability

James H. Noel
Clemson University

INFLUENCE OF BEAM ROTATION ON THE RESPONSE OF CANTILEVERED FLOW ENERGY HARVESTERS EXPLOITING THE GALLOPING INSTABILITY

A Thesis
Presented to
the Graduate School of
Clemson University

In Partial Fulfillment
of the Requirements for the Degree
Master of Science
Mechanical Engineering

---

by
James H. Noel
December 2017

Accepted by:
Dr. Mohammed F. Daqaq, Committee Chair
Dr. Gang Li
Dr. Paul Joseph

Abstract

Energy harvesters are scalable devices that generate microwatt to milliwatt power levels by scavenging energy from their ambient natural environment. Applications of such devices are numerous, ranging from wireless sensing to biomedical implants. A particular type of energy harvester is a device which converts the momentum of an incident fluid flow into electrical output by using flow-induced instabilities such as galloping, flutter, vortex shedding and wake galloping.

Galloping flow energy harvesters (GFEHs), which represent the core of this thesis, consist of a prismatic tip body mounted on a long, thin cantilever beam fixed on a rigid base. When the bluff body is placed such that its leading edge faces a moving fluid, the flow separates at the edges of the leading face causing shear layers to develop behind the bluff face. The shear layer interacts with the surface area of the afterbody. An asymmetric condition in the shear layers causes a net lift which incites motion. This causes the beam to oscillate periodically at or near the natural frequency of the system. The periodic strain developed near the base of the oscillating beam is then transformed into electricity by attaching a piezoelectric layer to either side of the beam surface.

This thesis focuses on characterizing the influence of the rotation of the beam tip on the response and output power of GFEHs. Previous modeling efforts of GFEHs usually adopt two simplifying assumptions. First, it is assumed that the tip rotation of the beam is arbitrarily small and hence can be neglected. Second, it is assumed that the quasi-steady assumption of

the aerodynamic force can be adopted even in the presence of tip rotation. Although the validity of these two assumptions becomes debatable in the presence of finite tip rotations, which are common to occur in GFEHs, none the previous research studies have systematically addressed the influence of finite tip rotations on the validity of the quasi-steady assumption and the response of cantilevered flow energy harvesters.

To this end, the first objective of this thesis is to investigate the influence of the tip rotation on the output power of energy harvesters under the quasi-steady assumption. It is shown that neglecting the tip rotation will cause significant over-prediction of the output power even for small tip rotations. This thesis further assesses the validity of the quasi-steady assumption of the aerodynamic force in the presence of tip rotations using extensive experiments. It is shown that the quasi-steady model fails to accurately predict the behavior of square and trapezoidal prisms mounted on a cantilever beam and undergoing galloping oscillations. In particular, it is shown that the quasi-steady model under-predicts the amplitude of oscillation because it fails to consider the effect of body rotation. Careful analysis of the experimental data indicates that, unlike the quasi-steady aerodynamic lift force which depends only on the angle of attack, the effective aerodynamic curve is a function of both the angle of attack and the upstream flow velocity when the effects of body rotation are included. Nonetheless, although the quasi-steady assumption fails, the remarkable result is that the overall structure of the aerodynamic model remains intact, permitting the use of aerodynamic force surfaces to capture the influence of tip rotation.

The second objective of this thesis is to present an approach to optimize the geometry of the bluff body to improve the performance of flow energy harvesters. It is shown that attaching a splitter plate to the afterbody of the prism can improve the output power of the device by as much as 60% for some cases. By increasing the reattachment angle of the shear layer and producing additional flow recirculation bubbles, the extension of the body using the splitter plate increases the useful range of the galloping instability for energy harvesting.

Dedication

To my family, for their unfailing support.

Acknowledgments

Many have helped me along the way, and I fear that an attempt to list them all would disrespect those that have helped in ways I haven't even seen. However, I must show my appreciation for the those that went above and beyond.

I thank Dr. Todd Schweisinger; not only did he put up with all my equipment in his lab for years, he went on to extend toward me kindness, friendship, and mentoring along the way.

Many heartfelt thanks to Dr. Ali Alhadidi for taking me under his wing and remaining patient with my undergraduate ignorance, correcting me without condescension and challenging me with grace.

Gwen Dockins and Kathryn Poole were constant lifesavers, taking care of all the paperwork that I never had to touch.

Thanks to Dr. James Gibert for generously offering me his time, helpful insights, and friendship whenever we would meet on the road.

With immense gratitude, I recognize Dr. Daqaq for providing this opportunity for me to grow, both academically and personally. While he spent untold time working with me on the technical aspects of this project, I am most appreciative of the time he invested in me.

I also acknowledge Clemson University and all those operating the Palmetto Cluster for the generous allotment of compute time.

I gratefully acknowledge support by the National Science Foundation under Grant CMMI-1335049.

Contents

List of Tables

List of Figures

Chapter 1

Introduction

When humans are exploring the boundaries of the visible universe and delving even further into the structure and relationship of subatomic particles, the topic of low-power energy harvesting does not receive much popular attention. In order to establish the relevance of this work and the significance of the results, some background will be laid regarding the need for energy harvesting, the operating principles of the energy harvester examined in this study, and the unique perspective adopted by the present work.

1.1 The Need for Energy Harvesting

Electrical power has been popularized as a "clean" alternative to fossil fuels and other combustibles. Electricity is a renewable resource which can be easily and safely stored and transported. However, the cleanliness of electrical power is entirely dependent on two factors: the equipment used to generate the power and the equipment used to store the power.

Currently, the primary sources of electrical power are nuclear, coal, and hydroelectric plants. When electrical devices are connected directly to local power grids supported by these plants, the cleanliness is only dependent on the source. In recent years, great strides have been made to improve the levels of pollutive output from these plants. Furthermore, an

increased drive to capture and convert ambient energy in the environment has motivated the innovation and implementation of clean, renewable generation methods such as wind farms, demonstrating that large-scale energy production can be free from continuous pollution or generation of hazardous waste. Pushing beyond the large turbines in wind farms, development continues on equipment to tap into other forces of nature as a source of electrical power, such as the transformation of the energy in ocean waves and strong currents. Solar energy, too, has been successfully captured in a wide variety of contexts using panels of photovoltaic materials.

In some remote areas, access to a power grid is either unreliable or completely unavailable. For these locations, it can be necessary to supplement or replace the dependence on the shared grid by creating a smaller local "grid" using wind, solar, or hydroelectric generation equipment. The choice of the appropriate type of equipment becomes a question of environmental context and scale. While the environment is largely outside the domain of the engineer's control, the scale of the system presents a significant engineering consideration, especially at small scales.

For mobile or otherwise "off-the-grid" devices with small power demands, the predominate method of supplying power is with batteries charged by a larger, external source grid [6, 7]. The unfortunate consequences of the seemingly inescapable dependence on batteries are twofold: (1) batteries wear out, fail, and must be replaced, and (2) batteries are typically environmentally harmful, both in production and disposal. The unending cycle of failure and replacement is more than a matter of convenience; such a cycle only exacerbates the negative environmental impacts of battery use. Furthermore, the separation of the generation and storage systems compounds the opportunity for energy loss due to the numerous conversions required to transmit energy to the final destination device.

For very small power demands, a unique alternative presents itself: each device might generate its own "grid" using energy scavenged from the environment [8]. The advantages of such a system are numerous, but the notable attraction is that the device could operate

without depending on a costly, inconvenient, and pollutive stream of battery replacements. The label Energy Harvesting (EH) is applied to systems which generate power on the milli- and micro- scale from ambient natural energy (solar, fluid flow, kinetic) or wasted energy in man-made processes (vibration).

1.2 Flow Energy Harvesters

A flow energy harvester (FEH) in particular is any device which converts the momentum of an incident fluid flow into electrical output. The working fluid is most commonly air or water due to their availability in nearly any environment, natural, or otherwise.

1.2.1 A problem of scale

As previously mentioned, the process of scaling energy generation systems can present a significant challenge, especially for FEHs. Traditional wind turbines, for example, turn an inductive generator. To demonstrate some fundamental limitations imposed on the scaling of this sort of generation, Faraday's law of induction can be considered, stated as

$$\varepsilon = -n\frac{d\Phi_B}{dt} \tag{1.1}$$

where ε is the induced voltage, n is the number of turns in the coil, t denotes time, and Φ_B is the magnetic flux of the system. For a constant surface and a uniform magnetic field, the magnetic flux through the surface can be defined as

$$\Phi_B = BA\cos\theta \tag{1.2}$$

where the magnetic field strength B passes through the coil area A at an angle θ to the area normal. When the characteristic radius of the coil is scaled by any factor κ, the modified

area scales as $A' = \kappa^2 A$. Therefore, any inductive coil scaled by a factor of κ will have its voltage output scaled by κ^2, without considering the other forms of scaling losses.

Furthermore, a second geometric constraint for FEHs in particular can be easily grasped through a review of the power contained in a certain amount of moving fluid. Power can be defined as a force acting with a certain velocity, or

$$P = \mathbf{F} \cdot \mathbf{v} \tag{1.3}$$

where P is power, $\mathbf{F}$ is a force, and $\mathbf{v}$ is a velocity. For a fluid flow, the force $\mathbf{F}$ can be idealized using the dynamic pressure, $\frac{1}{2}\rho V^2 A$, which upon substitution into Equation 1.3 gives

$$P = \frac{1}{2}\rho v^3 A \tag{1.4}$$

where ρ is the fluid density, v is the incident free-stream fluid velocity, and A is the cross-sectional area of the incident airflow. It is readily apparent that for any FEH geometrically scaled by a factor κ, the swept area (and thus the theoretical maximum available power) is scaled by κ^2. Not only is the ability of any inductive generator to convert translational or rotational energy to electricity decreased by a factor of κ^2 when the dimensions of the device are scaled by κ, the theoretical maximum fluid energy available to the generator is also decreased by a factor of κ^2.

This simplistic analysis ignores the nonconservative effects of friction, which are far more significant for smaller devices. It is known that drag losses are greatest at low Reynolds numbers [9]. At the smaller scale, the volume to surface area is very low: body forces such as lift are less effective as the surface effects of interface friction (e.g., that due to viscous drag and machine component interaction). The combination of decreased theoretical potential and increased physical losses results in the difficulty of producing small-scale wind energy generation systems.

1.2.2 Flow energy harvesting from cross-flow instabilities

Although the geometric constraints cannot be avoided, the nonconservative losses of a generation system can be reduced. For small scale FEHs, this can be accomplished by minimizing any relative motion between interfaces to reduce friction. This has made oscillating FEHs a promising solution.

Oscillating FEHs employ the natural elasticity of materials to provide a means of translation or rotation devoid of a sliding interface. Instead of relying upon a constant aerodynamic force to produce a deflection or rotation in a certain direction, oscillating FEHs take advantage of natural phenomena which provide periodic forcing. The three primary types of periodic aerodynamic forcing utilized are galloping [10], flutter [11], and vortex shedding [12].

Galloping is a self-exciting phenomena which operates on bluff bodies with a substantial afterbody. A body is identified as "bluff" when the surrounding flow is marked by distinct separation at the edges of the leading face. The shear layers which develop behind the bluff face interact with the surface area of the afterbody. An asymmetric condition in the shear layers causes a net lift which incites motion. An object is prone to galloping oscillation if it tends to increase the amount of net lift each subsequent cycle in response to the motion caused by the initial net lift. Oscillations occur at or near the natural frequency of the base system. The response will increase in amplitude until structural failure occurs or no additional energy per cycle can be drawn from the incident flow.

Flutter is similar to galloping, as both arise from similar physical mechanisms. However, the term flutter typically focuses on two degree-of-freedom (TDOF) plunge and pitch oscillations [13]. Furthermore, the frequency behavior diverges from that of simple one dimensional galloping, as the interaction of the two modes can cause significant shifts in the oscillation frequency. Traditionally considered in the case of airplane wings, flutter draws energy from the incident flow as a result of moments created from unevenly distributed lift

forces. Similar to single degree-of-freedom (SDOF) galloping, flutter propagates to the limits of the supporting structure or the limits of the aerodynamic instability of the oscillating body itself.

Vortex shedding from the trailing edges of bodies placed in incident flow can provide periodic forcing determined by the Strouhal number of the flow. The amplitudes generated by this phenomena tend to be smaller than the other two mechanisms; vortex street formation does self-propagate in an unstable manner to large amplitudes. Furthermore, the amplitude growth with respect to incident flow velocity is not a monotonically increasing function, as is the case for galloping and flutter. Vortex-induced oscillation is resonance-based and is therefore sensitive to a small range of incident flow velocities and Strouhal numbers. Values outside this range, whether high or low, will not result in effective energy transfer.

Energy can be extracted from these cross-flow instabilities using a variety of physical mechanisms. Traditionally, the flow energy is first converted into mechanical energy stored in a vibrating elastic element. Flutter has been exploited by mounting an airfoil on a cantilevered beam [14, 15, 16]. Additionally, when a thin "belt" is held in tension, flutter induces vibrations in the band [17]. Akaydin *et al.* demonstrated the method of placing a cantilever beam downstream of a fixed bluff body to harness vortex induced vibrations [18]. Mehmood *et al.* show an example implementation where the bluff body itself is free to oscillate on an elastic mounting [19].

Despite the successful exploitation of flutter and vortex shedding, the nature of galloping-based energy harvesting offers unique advantages. The focus of this study will be restricted to galloping flow energy harvesters (GFEH) consisting of a bluff body mounted on the tip of cantilever beams.

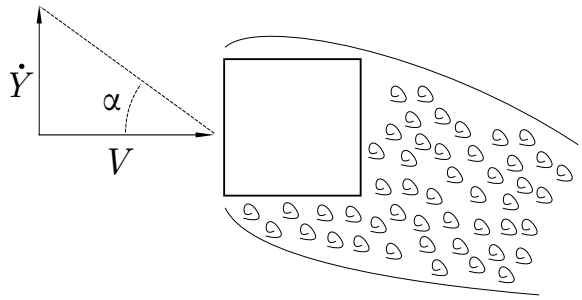

Figure 1.1: The fundamental operational principle of galloping is the flow asymmetry induced by body motion.

1.3 Principles of Galloping

Of the three periodic excitation methods mentioned, galloping is the preferred method due to the simplicity of designing a FEH which can undergo large-amplitude galloping oscillations as well as the relative insensitivity of the galloping instability to the flow velocity. The analysis of galloping is often traced to the pioneering observations of Den Hartog in the early 19^{th} century [20]. The early observations of Den Hartog related to the oscillations of electric power transmission lines with asymmetric geometry caused by the formation of ice around the circumference of the wire. The basic understanding illustrated that the production of lift requires asymmetry. For a body in motion, constrained to oscillate in one dimension, the incident flow vector has two components, as shown in Figure 1.1; the free-stream flow velocity V and the relative motion of the body $\dot{Y}$. If the body is asymmetric along the axis of incidence, a lift force vector will be produced. When the asymmetry is oriented such that a component of the lift acts in the same direction as the motion of the body, and the magnitude of that component grows as the body velocity grows, the system is prone to galloping oscillations. The effect is a velocity-dependent force which acts as an energy pumping mechanism, or as *negative damping*.

In the context of physical systems, damping is typically the component which subtracts energy from a system and creates an amplitude decay. Negative damping adds energy to the

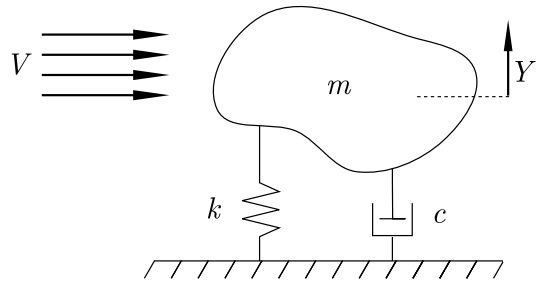

Figure 1.2: A single DOF galloping system.

oscillating system, causing amplitude growth. The presence of the negative aerodynamic damping in galloping does not eliminate the nonconservative realities in a physical oscillating system. In particular, an energy harvester is designed to remove energy from the oscillating system and convert it into electrical energy. In order to build oscillation amplitude and allow energy production capabilities, the negative damping must be sufficient to overcome the mechanical and electrical damping present in the harvesting system. The mathematical criteria necessary to activate galloping oscillations will be more specifically defined in Chapter 3.

The performance of a GFEH depends on a number of other factors, including the cut-in wind speed, the oscillation frequency, the amplitude of the resulting limit-cycle oscillations (LCO), hysteresis due to nonlinearities in the lift force, and the amplitude growth rate.

1.3.1 Translational galloping

By far the most widely researched topic is the translational galloping of bluff structures is when the bluff body is constrained to vibrate in translation along one axis without any rotation. These structures can be built on linear slides or using 4-bar mechanisms. Fundamental works by Parkinson [10, 21] set the groundwork for many investigations, followed by Nakamura [22, 23], and too many others to cite.

However, for energy harvesting, the stipulation of pure translation is difficult to meet, prompting many to approximate pure translation by using the small deflections of a long cantilever beam or the small rotations of a long radius arm, both scenarios that include small amounts of tip rotation. While these approximations have been used with some success with published aerodynamic models [24, 25], the application of a translational model to a flow field around a rotating body is tenuous.

1.3.2 Translational-torsional galloping

Many authors have examined both torsional galloping and coupled translational-torsional galloping: Blevins [26, 27], Nakamura [28], and Matsumoto [29] have all thoroughly treated the torsional/coupled translational-torsional galloping of square and rectangular prisms and all have found the translation-based aerodynamic model to be insufficient.

1.4 Thesis Objectives

The first objective of this work aims to identify the physical mechanisms at work when a galloping body is exposed to finite tip rotation. As a beam-mounted bluff body oscillates with medium to large amplitude, the tip rotation is not negligible. To the author's knowledge, no model has yet been formulated to capture the behavior of a galloping beam-mounted body with non-negligible tip rotation. Detailed analysis of the underlying physics lays the groundwork for future work developing a new, more robust aerodynamic model.

The second objective seeks to optimize the power output of GFEH using geometric modifications inspired by an understanding of the underlying physics. The steady-state behavior of traditional geometry is well documented: the history of the study of galloping has its roots in civil engineering interests, so the body of literature as it developed and grew over time focused on simple prisms and profiles commonly found on engineered structures.

However, the geometry most suitable for a GFEH may not fall into one of the above categories. It is therefore advantageous to identify the geometries which provide the greatest instability toward galloping and maximize the flow asymmetry to generate the most lift.

1.5 Thesis Outline

First, a review of bluff body aerodynamics identifies some known fluid mechanisms which operate on rotating bodies. Second, the traditional linearized beam model is compared with a large-displacement formulation to test the limits of the small angle assumption for modeling tip rotation. Third, experimental trials are presented to demonstrate the effects of body rotation on the aerodynamic forces. Fourth, the ideas presented in the preceding chapters come together to optimize the tip body geometry for maximum power. Finally, the major conclusions are discussed to open doors to the next steps in GFEH modeling.

Chapter 2

Bluff Body Aerodynamics

Fluid-structure interactions operate as highly complex, coupled systems. Fully simulating the behavior of a GFEH requires simultaneous solutions of the fluid and solid domains at each time step. While such systems can be solved with numerical packages, the computational cost often outweighs the benefits of the extreme precision. In order to construct a more accessible model for GFEH behavior, the flow around the tip body must be first understood and appropriately simplified.

It is assumed that all incident flow uniformly approaches the harvester parallel to the undeformed axis of the beam. While such a scenario is not commonly found in real-world environments, it sets a reasonable scope for harvester comparisons. The flow is also assumed to be smooth. Although galloping can be modeled under turbulent flow (for an example see Nakamura [22]), the present work is restricted to laminar flow conditions.

2.1 The Quasi-Steady Assumption

The analysis can be further simplified by the *quasi-steady assumption.* Under this assumption, the flow around a body in motion can be predicted using the known flow around a fixed body, provided two main criteria are met: a minimum velocity threshold and a similarity principle.

Loosely speaking, if the fluid velocity is fast with respect to the body motion, the flow impacting the body will not be influenced by its own wake at any point in its oscillation, removing any feedback from the body motion. Some debate has been held over the best threshold value of wind velocity V to give quasi-steady flow, labeled here V_{qs}. Païdoussis [30] documents the development of an approximate threshold, with Fung in 1955 giving a threshold $V_{\text{qs}} = 10 f_n D$, where f_n is the frequency of body oscillation in Hertz and D is the characteristic body width in meters [31]. Blevins agreed, for different reasons, in 1977 [26], but as a result of further work later increased the threshold value to $V_{\text{qs}} = 20 f_n D$ in a 1990 revision [13]. Furthermore, a more involved estimation of

$$V_{\text{qs}} = \frac{4 f_n D}{\text{St}}. \tag{2.1}$$

was suggested by Bearman *et al.* [32], taking into consideration the Strouhal number of the body, defined

$$\text{St} = \frac{f_s D}{V} \tag{2.2}$$

where f_s is the vortex shedding frequency for the geometry in question. This threshold appropriately aims to move the incident velocity far from a region where the vortex shedding would interact with the galloping behavior.

Beyond a simple threshold relationship between wind and body velocity, the second requirement is that the shape of the flow be fundamentally similar to that of the stationary case. When bluff bodies gallop in pure translation, one can simply select the body as a fixed reference frame and it is apparent that, provided the first criterion is met, the flow is indistinguishable from a steady scenario. The fluid impacts the "fixed" body with the both the velocity of the free-stream flow, V, and the body motion, $\dot{Y}$, at an angle α demonstrated

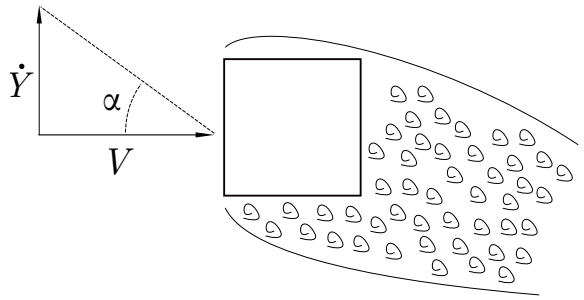

Figure 2.1: The induced angle of attack on a body in crossflow translation.

in Figure 2.1.

$$\alpha = \tan^{-1}\left(\frac{\dot{Y}}{V}\right) \tag{2.3}$$

Therefore, the force experienced by a body galloping in pure crossflow translation is traditionally approximated by using the steady-state force equation

$$F_N(\alpha) = \frac{1}{2}\rho V^2 A C_N(\alpha) \tag{2.4}$$

where ρ is the density of the fluid, A is the frontal area of the body ($A = DH$), and C_N is a dimensionless force coefficient defined as

$$C_N = C_{\text{lift}}\,\cos\alpha - C_{\text{drag}}\,\sin\alpha \tag{2.5}$$

where the subscripted N indicates the force normal to the top face of the body in the crossflow direction. Forces aligned with the flow are neglected because the body is fixed in that axis.

The similarity condition for quasi-steady flow is not so easily met in the present investigation, because the tip-mounted bluff body undergoes slight rotation as the beam deflects. Reviewing the means of lift force production in steady conditions lays the groundwork for understanding the influence of rotation.

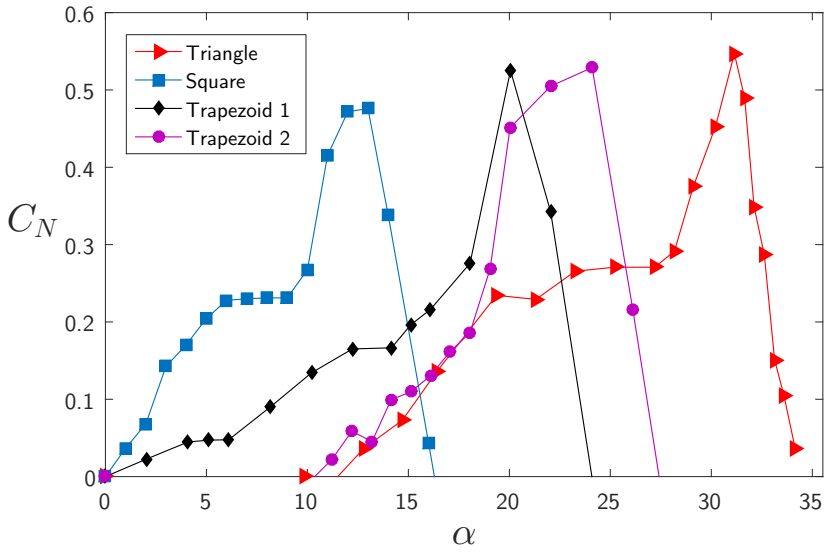

Figure 2.2: Variation of C_N with α for four bluff profiles with frontal width D facing the flow: a square (□), a trapezoid with a $0.75D$ rear face (◊), a trapezoid with a $0.5D$ rear face (○), and a 63°-27°-63° triangle (▷). Data from [1].

2.2 Transverse Force in Steady Conditions

A thorough review and explanation of the mechanism of lift on bluff bodies in crossflow was conducted by Luo *et al.* [1]. However, a brief summary is pertinent to set up the context for analyzing the flow around beam-mounted GFEH. Under steady conditions, the evolution of lift can be discussed in terms of the time-averaged behavior, neglecting the influence of rapidly shedding vortices. A bluff body causes flow separation from the leading edges of the side faces, as is sketched in the simple schematic in Figure 2.1. When $\alpha = 0$, the flow is, on average, symmetric. As the angle of attack increases, the upper shear layer draws closer to the upper face of the body, increasing the entrainment of fluid above the upper face. This leads to a net suction upward, producing lift.

As the angle of attack grows, the interaction with the side faces of the body influences trends in the lift production. Luo *et al.* notes that square bodies exhibit an inflection point in the lift curve caused by cycles of weak reattachment onto the upper face at some angles of attack [33]. This detail is observed between 5–10° for the square in Figure 2.2. A similar

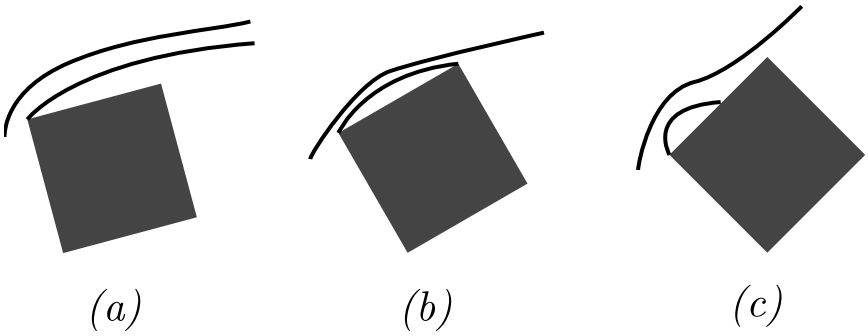

Figure 2.3: Flowlines are drawn around a square body at various angles of attack to demonstrate (a) weak suction when the shear layer is far from the side face, (b) strong suction from the large recirculation bubble, and (c) weak suction from the small recirculation bubble.

feature appears in the lift curve of the triangle and is likely due to a similar effect. At higher angles, the phenomena disappears and the lift resumes its upward trajectory.

Eventually an angle of attack is reached at which the upper shear layer has strong periodic reattachment to the trailing edge of the upper face. When the shear layer firmly connects to the trailing edge, maximum lift is achieved: the angle of reattachment offers the greatest shear layer curvature with the largest region of entrained fluid, as demonstrated in Figure 2.3.

The use of trapped vortices as lift-generating devices is well known in the case of delta wing aircraft [34]. The velocity of the trapped flow reduces the pressure exerted on the body. In the case of the bluff body, the faces of the body opposite to the trapped vortex are surrounded by the disturbed wake, a region of high pressure, driving the net lift. As the angle of attack increases beyond the reattachment angle, the point at which the flow reattaches shifts further toward the leading edge, shrinking the size of the recirculation bubble and decreasing the net lift. As the angle progresses further, the net force becomes negative.

Therein lies the self-limiting nature of galloping: a vibrating body experiences a positive net force below the reattachment angle of attack and negative net force significantly beyond that angle. Therefore, amplitude growth that reaches high angles of attack does not further

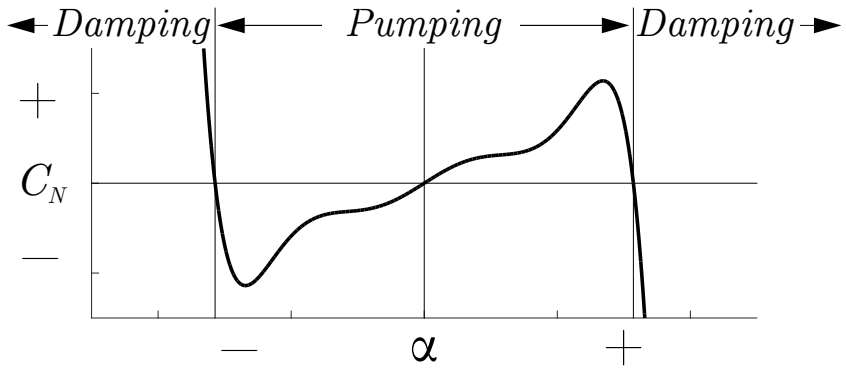

Figure 2.4: The aerodynamic effect on the dynamic system divided into regions of α.

pump up the oscillating system and is subdued.

When the lift is combined with the drag experienced by the body, the normal force coefficient curves can be plotted as in Figure 2.2. The shape of these curves can be interpreted as shown in Figure 2.4. The greater the area under the curve, the greater the effect of the "pumping" action. The zero crossing of the curve indicates the self-limiting tendency of galloping.

The evolution of the normal force can be correlated with geometric features of the bluff body. The square has the greatest width behind the front face, or the widest *afterbody*, and it experiences the most suction at lower angles of attack because its side faces start out very close to the separated shear layers. However, the same closeness which boosts flow interaction at low angles of attack also forces reattachment earlier: the square's C_N curve has its peak at the lowest angle. As the width of the afterbody shrinks, the lift at low angles of attack decreases due to weaker shear layer interaction while the angle of peak lift increases due to delayed reattachment. This trend is apparent in the shift of the curve for profiles with successively narrower afterbodies. Conversely, reattachment can be forced earlier than on the square if the afterbody is extended in the streamwise direction, as is the case with a rectangular bluff body. Kazakevich and Vasilenko report lift curves for a number of rectangular aspect ratios and the reattachment angle of attack monotonically decreases as

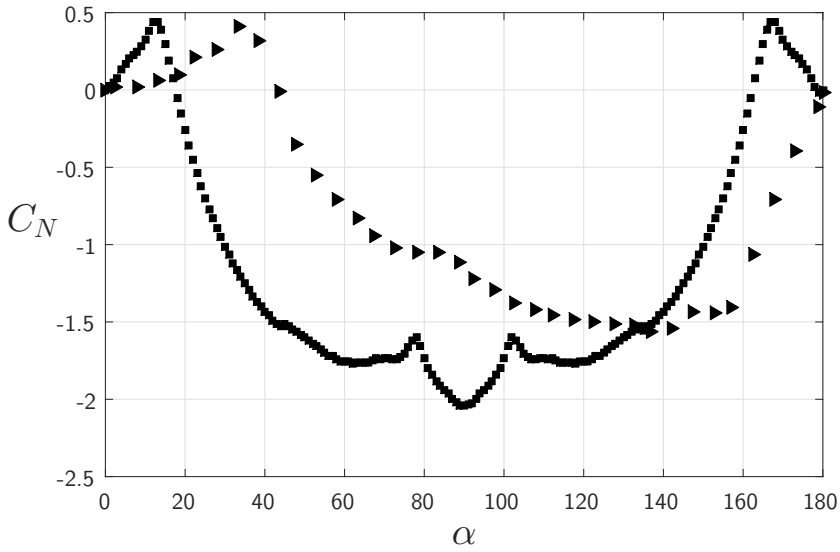

Figure 2.5: Variation of C_N with α for the square profile (square marker) and an equilateral triangle (triangle marker). Square data from Norberg and triangle data from Alonso [2, 3].

the streamwise length of the body increases [35].

According to Equation 2.5, at high angles of attack, the drag on the body becomes the dominant force contribution. The consequence can be observed in Figure 2.5, as the tapered triangular afterbody experiences less drag and, accordingly, a much broader range of angles which produce a net positive force.

In order to port empirical measurements into a mathematical model, an interpolating or fitted function is required. For numerical simulation, the complexity of the interpolating function is not critical, so high-accuracy methods such as Fourier Series or cubic spline interpolation may be used. However, in the interest of simplifying the model to the eventual end of deriving an approximate analytical solution, it is convenient to use an interpolating polynomial of the form

$$C_N = \sum_{j=1}^{m} A_j \, |\alpha|^j \, \mathrm{sgn}(\alpha) \tag{2.6}$$

where C_N is the normal force coefficient and A_j indicates the coefficient of the j^{th}-order term. The sign function provides the required symmetry for negative angles of attack.

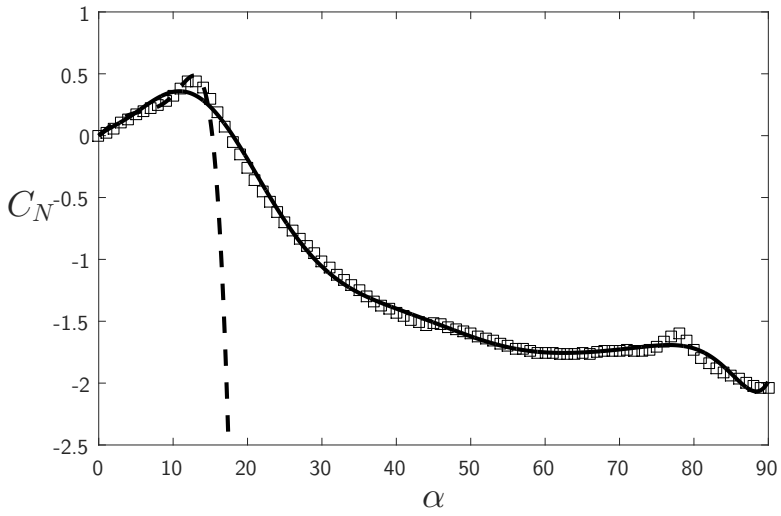

Figure 2.6: Fitted polynomials for the square data. Dashed line indicates odd 7^{th}-order polynomial. Solid line indicates 11^{th}-order polynomial.

Traditionally, odd 7^{th}-order polynomials are used to capture the forcing data. However, higher-order polynomials can be fitted if more detail is required from the model. To evaluate the usefulness of standard 7^{th}-order models, consider the data first presented in Figure 2.5 for the square profile.

Figure 2.6 demonstrates an 11^{th} order fit and a 7^{th}-order odd polynomial fit. The 7^{th}-order as provided by Parkinson captures very good detail until about $\alpha = 14°$ at which point it directly abandons the true path of the data. Conversely, the higher order polynomial smooths over some detail at low angles while providing good fit even until $\alpha = 90°$. The appropriate fitted model must be selected based upon the demands of the context.

2.3 Unsteady Effects of Body Rotation

The rotation of the faces into the wind induces a circulation not encountered by a stationary body in uniform flow and not captured by a single angle of attack. Torsional galloping cases do not reflect quasi-steady behavior due to this circulation. Nakamura examined the effectiveness of standard galloping models for torsional vibration and noted that quasi-steady

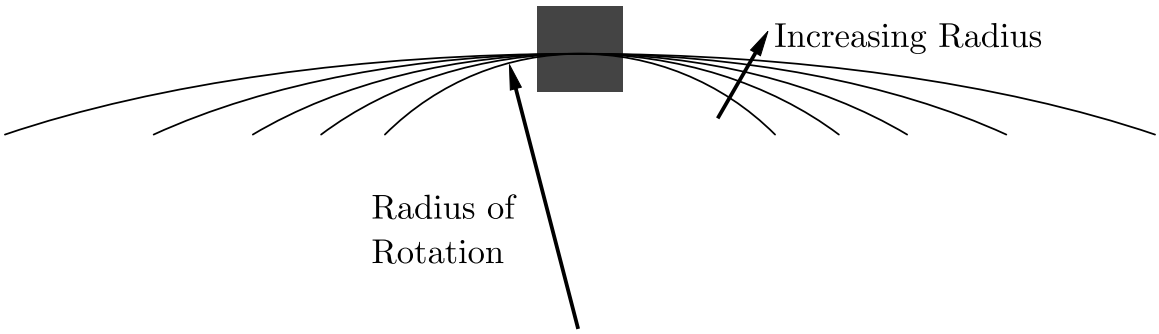

Figure 2.7: Schematic demonstrating how increasing the radius of rotation straightens the path traveled by a vibrating body around its equilibrium position.

models were only applicable if the radius of rotation extended far beyond the body; the effects of the circulation decrease as the trajectory of the body straightens [36] The straightening of the path traveled by the body is demonstrated in Figure 2.7.

B.W. van Oudheusden explored the effects of rotation on a galloping square body in a series of papers examining a body mounted on the tip of a rigid, rotating beam [37, 38, 39]. He found that quasi-steady theory tends to underpredict the amount of force experienced by a body undergoing simultaneous translation and rotation. Kluger *et. al* also observed a similar departure from quasi-steady theory with a cantilevered system (with significant tip rotation) [40]. The error shrinks when the rotation of body is slow with respect to the free-stream velocity. This trend should be expected, as pure translation (for which the quasi-steady assumption holds) could be viewed as the limit case of infinitely slow rotation.

The failure of quasi-steady theory for rotating bluff structures is not a new problem, and several researchers have used a transient model in limited contexts. Scanlan is widely referenced for his work developing the unsteady airfoil lift functions of Wagner and Theodorsen for applications to bluff structures [41]. Whereas Wagner noted that lift production on a suddenly rotated airfoil slowly ramped up to its steady state value, Scanlan found that bluff structures (*i.e.* a bridge deck) experienced an initial *overshoot* of the steady-state lift that slowly decreased to the steady value. While Scanlan's functions are limited to small angles

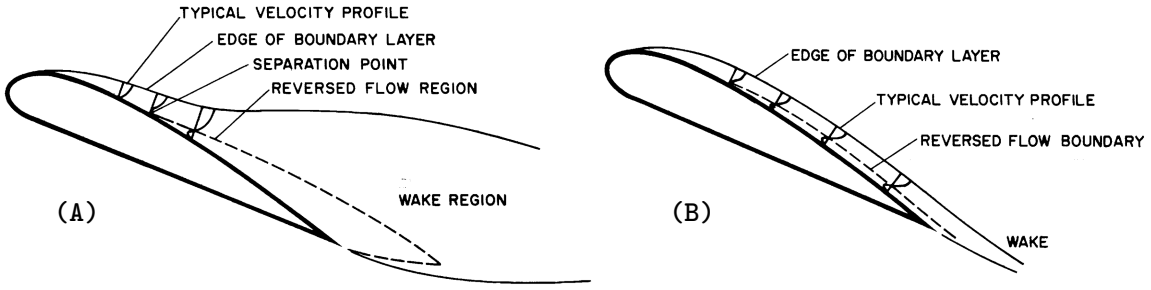

Figure 2.8: Comparison of typical early stall behavior for (a) static and (b) rotating cases (clockwise rotation). Figure from [4]. Document in public domain.

of attack, his observations provide a strong basis for deeper investigation.

The underlying mechanism responsible for the lift overshoot might be explained through a look at another branch of unsteady airfoil theory. It is well known that an airfoil in constant pitching rotation can experience dramatic increases in maximum lift production due to a phenomenon known as *dynamic stall*. For airfoils in static conditions, stall occurs at an angle of attack where flow over the wing separates and the airfoil experiences a condition of high drag and low lift. A dynamic stall, on the other hand, is a highly complex, time-dependent process. Figure 2.8 compares the onset of stall in the static case and the dynamic case.

In Figure 2.8.(a), the typical static stall case is characterized by a broad wake and a thick area of reversed flow. A stark contrast is observed in Figure 2.8.(b), where the boundary layer follows the profile of the airfoil closely, maintaining a very narrow wake region. In a static stall, the wide wake and reversed flow region allow for significant pressure recovery which dramatically cuts the upward suction leading to lift. The dynamic stall scenario visibly maintains a flow pattern mimicking pre-stall flow curvature, yet to an advanced degree which allows lift production to continue beyond angles allowed in a static case. It is important to note that the direction of pitching rotation is critical: pitching into the separated flow (clockwise for airfoils) causes the behavior pictured in Figure 2.8, while pitching away from the separated flow causes an opposite effect: increasing the flow separation and decreasing the lift force.

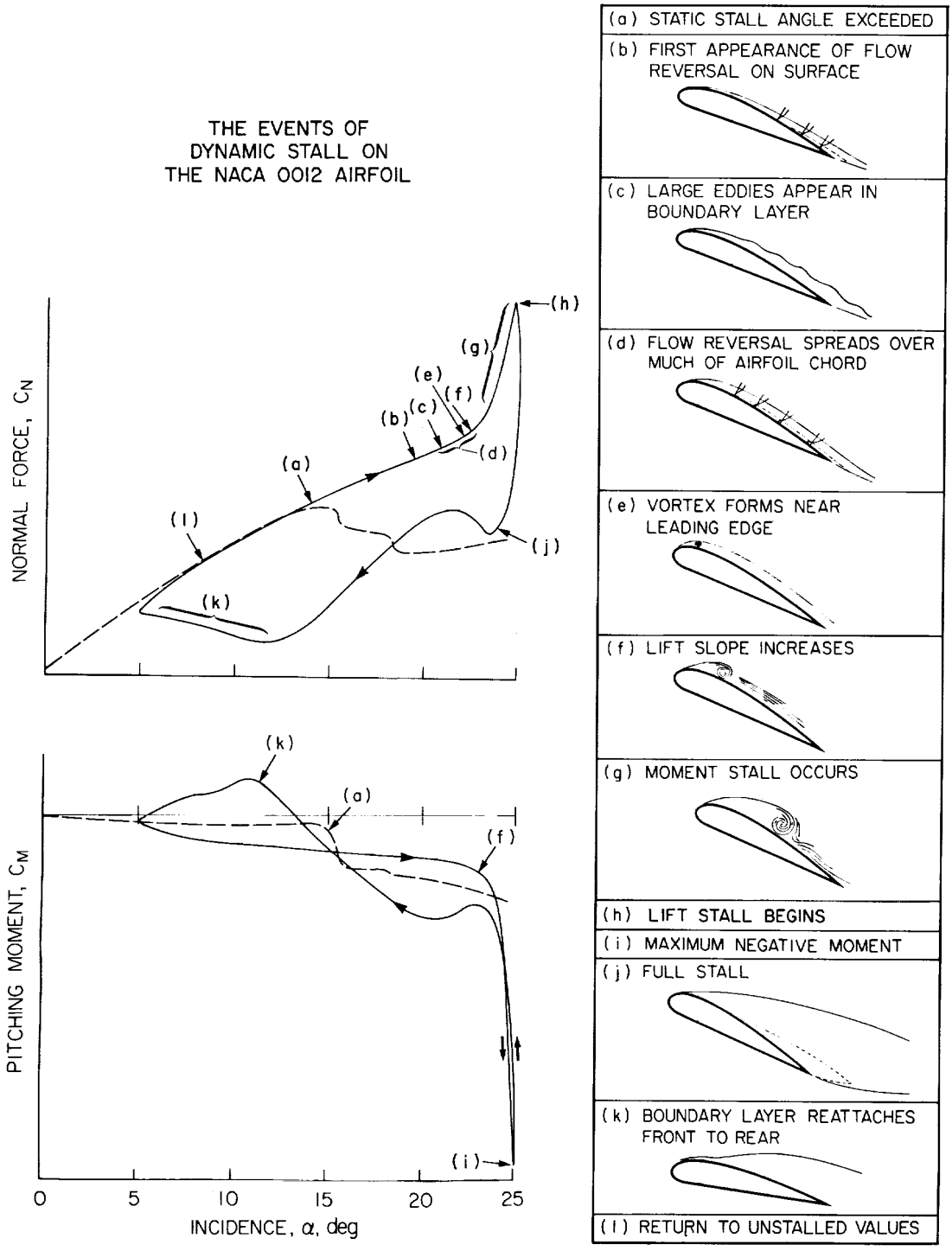

Figure 2.9: Development of dynamic stall on a NACA 0012 airfoil in sinusoidal motion $\alpha = 15° + 10° \sin \omega t$. Dashed lines in plots represent steady case values. Figure from [4]. Document in public domain.

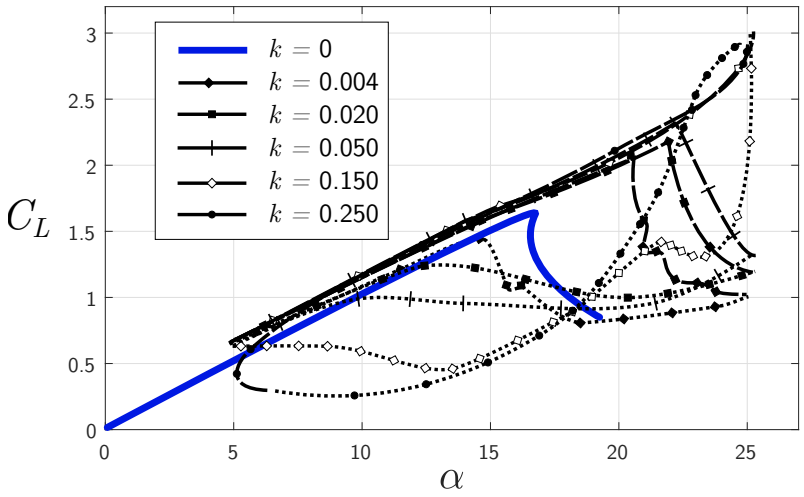

Figure 2.10: Effect of rotation on instantaneous lift production of a NACA 0012 airfoil. Dashed line indicates clockwise rotation, dotted line indicates counterclockwise rotation. Data from [5].

As the airfoil progresses further beyond the angle of static stall, the behavior enters the "deep stall" regime. The development of deep stall is broken down in Figure 2.9. Up until the angle of static stall (a), the lift behavior does not significantly deviate from the static case. As previously demonstrated, the early dynamic stall behavior continues on the same trajectory as pre-stall lift production until point (e), at which a leading edge vortex (LEV) begins to form as the airfoil reaches its peak angle of attack and slows down. The formation of an LEV continues to grow and impart suction on the upper face, causing the spike in lift coefficient. Because the LEV develops over time, its growth and eventual shedding operates with a delay behind the airfoil motion [42]. This lag causes the later stages of dynamic stall to be weakly dependent on the instantaneous position and rotation and strongly dependent on the reduced pitching frequency (oscillation frequency normalized by the chord length and free-stream velocity) and pitching amplitude [42, 43].

Figure 2.10 demonstrates the effect of varying the reduced pitching frequency $k = {}^{\omega c}/_{V}$ where ω is the oscillation frequency, c is the chord length, and V is the free stream flow velocity. In general, an increase in k tends to increase the maximum lift produced due to

the increasing strength of the LEV and the exaggerated curvature of the shear layers over the separated region. However, k has little effect on the behavior at angles far from the peak. Kramer identified a linear relationship between pitch rate and maximum lift for several airfoils in 1932, but McCroskey observed that there may exist a pitching frequency after which the strength of the LEV stabilizes [42, 44].

Although the above discussion directly pertains to airfoils, the mechanism at work in dynamic stall appears to explain the error in applying the quasi-steady assumption to a galloping oscillator with tip rotation. Of course, flow around bluff bodies has little resemblance to that around airfoils. However, McCroskey notes that airfoils with sharp leading edges (and the accompanying sharply separated flow) tend to experience more dramatic unsteady effects [42].

Another indication that bluff bodies may undergo dynamic stall effects comes from Oudheusden's observations that the quasi-steady assumption was least valid at conditions of low reduced wind speeds and high amplitude—in the present context, such conditions demonstrate high k and high pitching speed, the conditions optimal for dynamic stall. As the reduced wind speed grew (shrinking k) or the amplitude was reduced with damping (low pitching velocity), the quasi-steady assumption became more accurate.

Previously, it was noted that the direction of rotation has significant effects on the behavior of a body in dynamic stall: rotation away from the lifting surface can hinder performance. Airfoils are designed so that the upper surface experiences the suction of lift, so it's simple to state the direction of rotation that benefits lift performance. Bluff bodies experience lift on alternating faces when enduring galloping oscillation, so maximizing the effect of dynamic stall requires that the rotation of the body be synchronized with the alternation of lifting surfaces. Galloping requires lift production on the face leading into the incident flow. Therefore, the change of angle of attack must be in phase with the angular velocity of the body. The exact relationships for angular deflection of a cantilevered tip

Figure 2.11: Dye injection photograph of flow around square cylinder at 13° incidence. Re = 4900.

body will be discussed later, but at present it is sufficient to say that when the tip of the beam faces into the incident flow, the rotation is always at least partially in-phase. Some corroboration is given by Koide *et al.*, who compared three different mounting mechanisms for a galloping square body: one with zero body rotation, one with in-phase body rotation, and one with out-of-phase body rotation. He found that the in-phase configuration had vastly greater galloping output than the zero rotation case and both had greater response than the anti-phase case [45].

Flow visualization confirms some of the flow features expected from unsteady airfoil theory. A square prism was placed in a water tunnel at Re $\approx$ 4900. Figure 2.11 displays the flow over the lifting surface at $\alpha = 13°$ in a steady flow scenario. Dye was injected under the boundary layer to highlight the width of the recirculation region.

As seen in Figures 2.12a and 2.12b, the effect of rotation is to severely compress the width of the separated flow region, an effect expected from a review of dynamic stall. Although not pictured, the opposite effect was observed on the lower face of the square: rotation tended to widen the wake, also in keeping with the decrease of lift observed on airfoils rotating away from the lifting surface (dotted lines in Figure 2.10). Furthermore, the "LEV" for the bluff body is seen to form on the rear face; instead of increasing lift, the vortex will decrease pressure on the rear face and increase the drag. However, the effect of rotation is highly sensitive to the exact time history of α [42]. Therefore, the flow visualization presented

(a) Dye injected under the boundary layer.

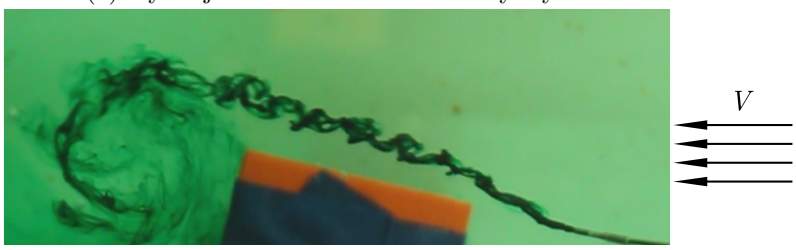

(b) Dye injected above the boundary layer.

Figure 2.12: Dye injection photograph of flow around square cylinder at 13° incidence. Re = 4900. CCW rotation at $\omega = 2\,\text{rad/s}$ ($k = 0.8$).

here should count only as a qualitative demonstration of the dramatic breakdown of the quasi-steady assumption in the presence of body rotation.

In areas such as helicopter dynamics where design considerations must include dynamic stall effects, it is traditional to empirically determine correction factors to augment quasi-static models [46]. To the author's knowledge, no standardized model yet exists for treating correction factors, as a number of research and design organizations each use proprietary approaches. Researchers in other fields have developed augmented quasi-steady models to accommodate rotation: Dickinson and Sane have successfully used their model to describe insect wing aerodynamics, but the trends bear little resemblance to bluff body flow [47, 48, 49, 50]. Therefore, it is of interest to identify trends present in the response of cantilevered galloping flow energy harvesters with non-negligible tip rotation. To this end, a model will be developed using quasi-steady aerodynamics and the feasibility of applying correction factors will be assessed by experimental evaluation.

Chapter 3

Including Beam Kinematics in the Harvester Model

The physical system is composed of a prismatic tip body mounted on a long, thin cantilever beam fixed on a rigid base. Geometric additions to the bluff body can be added, as in the case of the tail fin pictured in Figure 3.1. The transduction method employed in this system uses a Macro Fiber Composite (MFC) piezoelectric patch designed for energy harvesting applications. The patch is laminated to one (or both) sides of the beam and thin leads are connected to the desired load.

Traditionally, galloping has been modeled using a SDOF in the crossflow direction with linear restoring forces and simple viscous damping elements, and this approach has been validated repeatedly for pure translation (and small angle approximations of it) [25, 51, 52]. Bibo derived a model for the beam-mounted harvester without the presumption of small deflections, but the full order model was not applied in his study [15].

When the angle of tip rotation is not suppressed to be arbitrarily "small," the validity of the small angle assumptions previously used in harvester models is dubious. The aerodynamics of galloping are described primarily by the angle of attack with which the flow impacts the

tip body. The angle of attack is a combination of a relative velocity component and the tip rotation of the beam. Therefore, the accuracy with which the model predicts the tip rotation directly impacts the accuracy of the harvester model.

This chapter quantifies the error introduced by the traditional simplifications and proposes an analytical approximation to include the kinematic effects of tip rotation in Bibo's model.

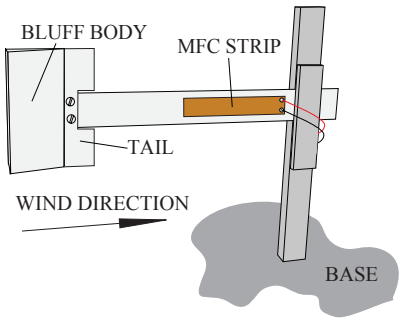

Figure 3.1: A sketch of the typical beam-mounted harvester implementation.

3.1 Deflection of Slender Beams

The beams employed by typical GFEHs are thin with respect to the length of the beam L, as pictured in Figure 3.2, to allow for large amplitude oscillation without incurring significant stress and fatigue at the base. Furthermore, it is helpful to keep the in-to-plane height of the beam narrow with respect to its width, so that the cantilever truly behaves as beam and not as a plate. To this end, the length should be at least 10 times the height. As the beam is only constrained at one end, it can be accurately treated as inextensible. The cross section and material properties of the beam can be considered constant along the length, as any laminated elements are small and thin and do not significantly affect the deflection shape of the beam.

The preceding assumptions allow the Euler-Bernoulli beam model to be used with good accuracy. The equation of motion in time t and arc-length s for a cantilever Euler-Bernoulli

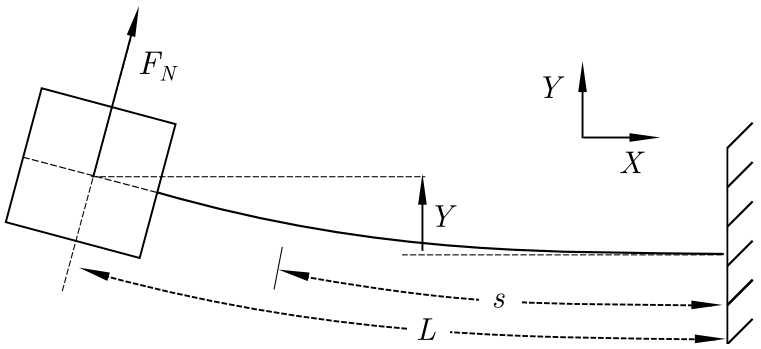

Figure 3.2: Beam coordinates.

beam including up to cubic nonlinearities is [15]

$$\eta_b \ddot{Y} + EIY'''' = -EI(Y'(Y'Y'')')' - \eta_b \left(Y' \frac{\partial^2}{\partial t^2} \left[\int_L^s \int_0^s (Y')^2 \, \mathrm{d}s \, \mathrm{d}s \right] \right)' \tag{3.1}$$

where primes denote spatial derivatives and overdots denote time derivatives. The right-hand side of the equation collects the nonlinear terms. The physical parameters are provided as follows: η_b is the mass per length of the beam, E is the Young's Modulus of the beam, and I is the area moment of inertia of the beam's cross section.

The tip mass on the harvester creates the linear boundary conditions

$$\left[EIY'' + I_t \ddot{Y}' \right]_{s=L} = 0, \qquad \left[EIY''' - M_t \ddot{Y} \right]_{s=L} = 0 \tag{3.2}$$

where M_t is the mass of the tip body and I_t is the mass moment of inertia of the tip body.

3.1.1 Linear Analysis

Erturk and Inman provide the derivations of the modal discretization for the linearized equation of motion for a beam with a connected tip mass [53]. Without repeating the work

here, the displacement can be expressed as a discretized function as

$$Y(s,t) = \sum_{n=1}^{\infty} \Phi_n(s) q_n(t) \tag{3.3}$$

where $q_n(t)$ are the unknown temporal functions,

$$\Phi_n = A_n \left[\cos\left(\lambda_n \frac{s}{L}\right) - \cosh\left(\lambda_n \frac{s}{L}\right) + \Xi \left(\sin\left(\lambda_n \frac{s}{L}\right) - \sinh\left(\lambda_n \frac{s}{L}\right) \right) \right] \tag{3.4}$$

are the linear mode shapes of a cantilever beam, and

$$\Xi = \frac{\sin(\lambda_n) - \sinh\left(\lambda_n \frac{s}{L}\right) + \lambda_n \frac{M_t}{\eta_b L} \left(\cos(\lambda_n) - \cosh\left(\lambda_n \frac{s}{L}\right) \right)}{\cos(\lambda_n) + \cosh\left(\lambda_n \frac{s}{L}\right) - \lambda_n \frac{M_t}{\eta_b L} \left(\sin(\lambda_n) - \sinh\left(\lambda_n \frac{s}{L}\right) \right)} \tag{3.5}$$

A_n is the modal constant resolved by mass normalization using Equation 3.6,

$$\eta_b \int_0^L \Phi_n^2 \, \mathrm{d}s + M_t \left(\Phi_n(L)\right)^2 + I_t \left(\Phi_n'(L)\right)^2 = 1 \tag{3.6}$$

and λ_n is the n^{th} root of the following characteristic equation:

$$\begin{aligned} 1 + \cos\lambda \cosh\lambda + \lambda \frac{M_t}{\eta_b L} (\cos\lambda \sinh\lambda - \sin\lambda \cosh\lambda) \\ -\lambda^3 \frac{I_t}{\eta_b L^3} (\cosh\lambda \sin\lambda + \sinh\lambda \cos\lambda) \\ +\lambda^4 \frac{M_t I_t}{\eta_b^2 L^4} (1 - \cos\lambda \cosh\lambda) = 0 \end{aligned} \tag{3.7}$$

In the absence of damping, the temporal function $q_n(t)$ can be expressed as

$$q_n(t) = B_n \cos(\omega_n t + \beta_n) \tag{3.8}$$

where B_n is a constant amplitude determined by initial conditions, β_n is a constant phase

shift fixed by initial conditions, and ω_n is found by

$$\omega_n = \frac{\lambda_n^2}{L^2}\sqrt{\frac{EI}{m}} \tag{3.9}$$

3.1.2 Nonlinear analysis

Just as in linear analysis, a nonlinear "mode" defines a shape function to describe the beam deflection. Treating the nonlinear terms in a weakly nonlinear system can use a variety of approaches, including perturbation methods [54, 55, 56] and invariant manifold construction [57]. The present work will adopt Nayfeh's treatment based on the method of multiple scales [54].

In linear analysis, each mode has a unique frequency of vibration. However, the beam nonlinearities introduce crosstalk between the modes such that the "normal mode" at one linear frequency can be expressed as some linear combination of all the beam's mode shapes. Therefore, the nonlinear response can be approximated by examining nonlinear interaction between the linear modes presented in the preceding section.

The first step is nondimensionalizing the equation of motion, Equation 3.1, with the following relations

$$y = \frac{Y}{L}, \qquad \hat{t} = t\frac{1}{L^2}\sqrt{\frac{EI}{\eta_b}}, \qquad \hat{s} = \frac{s}{L}$$

to get

$$\ddot{y} + y'''' = -(y'(y'y'')')' - \left(y'\int_1^{\hat{s}}\int_0^{\hat{s}} \dot{y}'^2 + y'\ddot{y}'\,\mathrm{d}\hat{s}\,\mathrm{d}\hat{s}\right)' \tag{3.10}$$

At this point, the discretization can be substituted into the equation of motion. Performing the substitution, multiplying by a mode shape function Φ_j, and integrating over the length of the beam forms the j^{th} modal equation of motion

$$\sum_{k=1}^{\infty}\ddot{q}_k\int_0^1 \Phi_j\Phi_k\,\mathrm{d}\hat{s} + \sum_{k=1}^{\infty} q_k\int_0^1 \Phi_j\Phi_k''''\,\mathrm{d}\hat{s} = -\sum_{k=1}^{\infty} q_k^3 g_{1,jk} - \sum_{k=1}^{\infty}(q_k\dot{q}_k^2 - \omega_k^2 q_k^3)g_{2,jk} \tag{3.11}$$

where

$$g_{1,jk} = \int_0^1 \left[\Phi_j \left(\Phi_k' \left(\Phi_k' \Phi_k'' \right)' \right)' \right] \mathrm{d}s \tag{3.12}$$

$$g_{2,jk} = \int_0^1 \left[\Phi_j \left(\Phi_k' \int_1^s \int_0^s \Phi_k'^2 \, \mathrm{d}s \, \mathrm{d}s \right)' \right] \mathrm{d}s \tag{3.13}$$

Applying the orthogonality conditions, the influence of the tip mass can be observed on the equation of motion [53]

$$\begin{aligned} &\sum_{k=1}^{\infty} \ddot{q}_k \left(\delta_{jk} - M\Phi_j(1)\Phi_k(1) - I\Phi_j'(1)\Phi_k'(1) \right) \\ &\quad + \sum_{k=1}^{\infty} \omega_k^2 q_k \left(\delta_{jk} - M\Phi_j(1)\Phi_k(1) - I\Phi_j'(1)\Phi_k'(1) \right) \\ &\qquad = -\sum_{k=1}^{\infty} q_k^3 g_{1,jk} - \sum_{k=1}^{\infty} (q_k \dot{q}_k^2 - \omega_k^2 q_k^3) g_{2,jk} \end{aligned} \tag{3.14}$$

where

$$M = \frac{M_t}{\eta_b L}, \qquad I = \frac{I_t}{\eta_b L^3}, \tag{3.15}$$

and δ_{jk} is the Kronecker Delta function comparing j and k.

If the tip mass and inertia ratios are small, the equation in q retains only weak modal coupling terms on the right hand side of Equation 3.16.

$$\ddot{q}_j + \omega_j^2 q_j = -\sum_{k=1} q_k^3 g_{1,jk} - \sum_{k=1} (q_k \dot{q}_k^2 - \omega_k^2 q_k^3) g_{2,jk} \tag{3.16}$$

Without repeating the derivations previously published in Nayfeh's papers [54, 55], the modal time function can be approximated by

$$q_k(t) = a_k \cos\left(\omega_{N,k} t + \beta_k\right) + \frac{g_{1,kk} - 2\omega_k^2 g_{2,kk}}{32\omega_k^2} a_k^3 \cos\left(3\omega_{N,k} t + 3\beta_k\right) \tag{3.17}$$

where β_k is a constant phase shift, a_k is the modal amplitude parameter, and

$$\omega_{N,k} = \omega_k + \frac{1}{8\omega_k}\left(3g_{1,kk} - 2\omega_k^2 g_{2,kk}\right) a_k^2 \tag{3.18}$$

to give a total displacement

$$y_k(s,t) = \Phi_k q_k + \sum_{j\neq k}^{\infty}\left[\Phi_j\left(\Gamma_{1,jk}q_k^3 + \Gamma_{2,jk}q_k\dot{q}_k^2\right)\right] \tag{3.19}$$

where

$$\Gamma_{1,jk} = \frac{1}{\Delta_{jk}}\left[\left(7\omega_k^2 - \omega_j^2\right)g_{1,jk} - \left(5\omega_k^2 - \omega_j^2\right)\omega_k^2 g_{2,jk}\right] \tag{3.20}$$

$$\Gamma_{1,jk} = \frac{1}{\Delta_{jk}}\left[6g_{1,jk} - \left(3\omega_k^2 + \omega_j^2\right)\omega_k^2 g_{2,jk}\right] \tag{3.21}$$

$$\Delta_{jk} = \left(\omega_k^2 - \omega_j^2\right)\left(9\omega_k^2 - \omega_j^2\right) \tag{3.22}$$

The k^{th} nonlinear "mode" shape is time varying; however, the shape at maximum deflection can be retrieved by maximizing q_k in time.

As seen in Equation 3.19, for large displacements, a cubic interaction arises between the mode of interest Φ_k and the remaining modes Φ_j. The nonlinear displacement reduces to the linear solution as the nonlinear terms $g_{1,jk}$ and $g_{2,jk}$ go to zero.

3.1.3 Error in Linearization

It is convenient to describe the beam tip rotation θ as a function of the dimensionless tip displacement y.

$$\theta = \xi y \tag{3.23}$$

The variation of ξ as predicted by the linear and nonlinear models is presented in Figure 3.3 for a variety of tip mass ratios M. It can be seen that in the presence of any tip mass, when the inertial load is concentrated on the tip of the beam, the value of ξ remains close

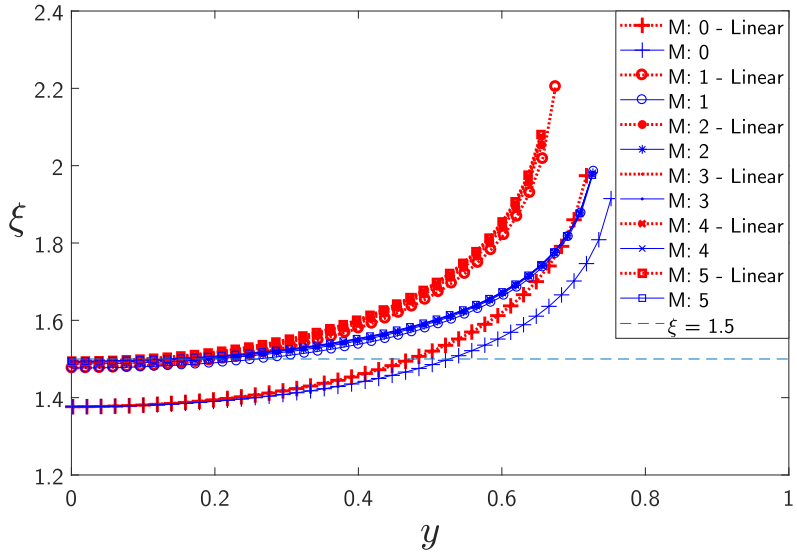

Figure 3.3: Variation of ξ with tip amplitude y.

to a constant 1.5 for a broad range of y ($0 \lesssim y \lesssim 0.3$). The nonlinear prediction actually demonstrates that the constant value approximation is more valid than initially expected from a linear analysis.

Figure 3.3 only represents a relative comparison. To evaluate accuracy, the linear and nonlinear analysis using the first bending mode will be evaluated against a fully nonlinear numerical simulation of a slender cantilever beam excited at its first natural frequency using ANSYS APDL. A fully nonlinear transient solution employed 30 nonlinear elements in the beam and a "dummy" element to simulate a variable tip mass. Arbitrary system parameters were selected to observe the deviation of the nonlinear simulation from the approximation. Although there were negligible differences in the results when tip inertias where modulated within the range normally seen in harvesters, all trials were normalized for tip inertia to reduce the degrees of freedom in the data. The code used is given in Appendix B. The results are presented in Figure 3.4.

It can be seen that the linear and nonlinear estimations coincide at low amplitudes. The increased error at lower M values is likely due to the error of a single-mode approximation:

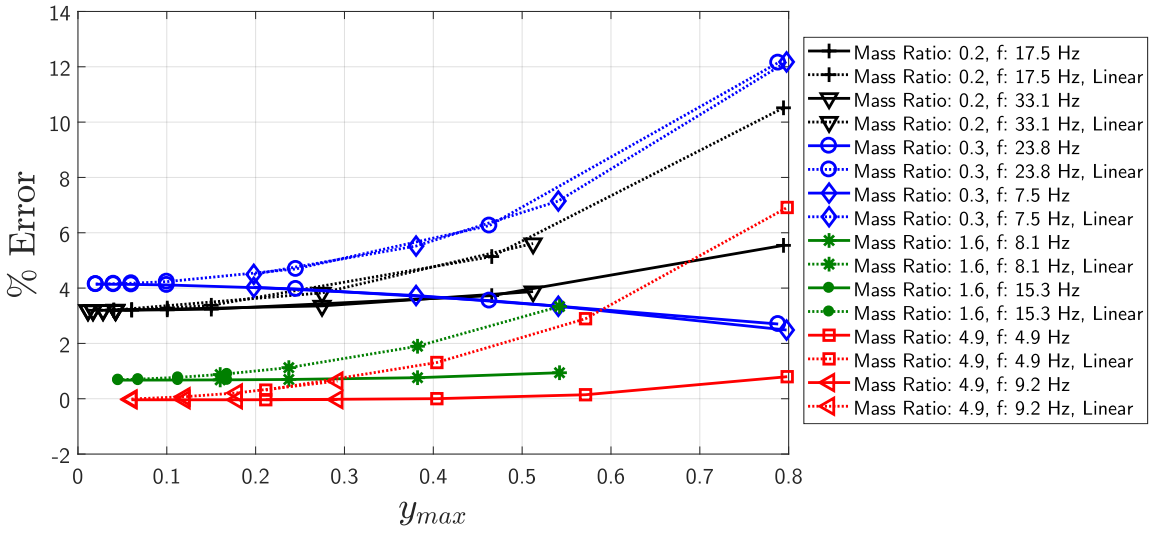

Figure 3.4: Maximum percent error in the angle of tip rotation as compared to the numerical simulation.

as the mass ratio increases, the inertia of the concentrated tip mass interacts with the first mode directly and the influence of higher-order harmonics decreases.

As could be expected, the nonlinear approximation provides a very good estimate of the tip rotation. However, the linear approximation is quite sufficient for a broad amplitude range, even beyond the point at which the small angle approximations would be expected to fail. Furthermore, the error is especially small for systems with a concentrated tip mass on the order of the beam mass. Therefore, the linearized approximation $\xi = 1.5$ can be used confidently even for medium-amplitude vibrations. The linear mode shapes can also be used to describe the kinematics and strains of the vibrating beam.

3.1.4 Beam Damping

Any realistic model of a vibrating beam must account for the energy lost through damping. The mechanisms of damping can vary from thermal dissipation to imperfect mounting fixtures to air resistance. Damping is most accurately identified through experimental means by observing the free response decay of a system in which damping is the only unknown

parameter.

In the present system, the identification of damping is not straightforward, as the damping in the system can be decomposed into structural (or material) damping and the damping due to still air. While it may seem reasonable to neglect the influence of air damping, Sugino's experiments with a vibratory energy harvester in variable atmospheric pressure suggest otherwise [58]. While it is tempting to roughly approximate the total damping as linear, the error introduced by a miscalculation of the damping ratio can be astronomical, as discussed in Appendix C.

Unfortunately, the influence of air cannot be accommodated by lumping all energy-draining effects into a single damping function. Woolam reviewed prior work on the still air damping of oscillating 2D flat plates and noted a consensus that unsteady vortex shedding is likely the primary mechanism at work [59]. Vortices shedding over the top and bottom of the plate create a large pressure differential, and no time is allowed for the recovery of base pressure as in a fully formed, steady wake. This phenomenon is easily seen in the photographs provided by Keulegan and Carpenter [60]. Because of the minimum flow velocity criterion for quasi-steady flow, where any wake disturbances due to system motion are swept downstream before they can significantly influence the system dynamics, the damping of vibrating cantilever beams in still air should not appear in the model when the incident flow is nonzero.

This requirement poses a significant experimental challenge: each system would need to undergo tests both in normal atmospheric pressure conditions as well as in a vacuum chamber to identify the damping influence of still air. However, approximations can be made using insight from the work of Baker *et al.*, who studied the free response of cantilever beams as the ambient air pressure was varied [61]. Using the traditional linear viscous damping model, where damping forces are proportional to velocity, it was found that the material damping of slender metallic cantilever beams was a very weak function of oscillation amplitude and a

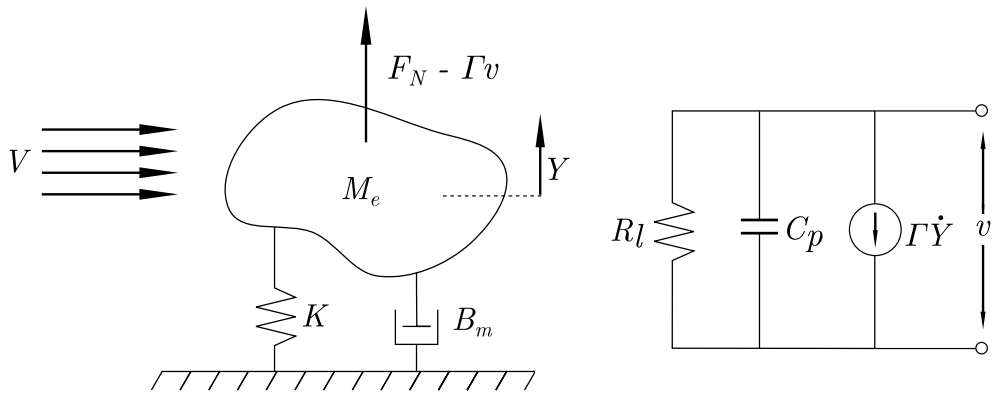

Figure 3.5: Schematic of linearized harvester model.

strong function of frequency. The aerodynamic damping, on the other hand, was strongly influenced by oscillation amplitude and Baker observed the traditional form of aerodynamic force calculations where the force is proportional to the square of the velocity. Therefore, the effect of material damping can be approximately isolated by neglecting the quadratic damping components observed in the free response decay.

Typically, the velocity in question would be the Y direction beam velocity. However, large deflections have non-negligible X direction motion, and any damping quantity should reflect this extension. Therefore, the present beam model will employ an experimentally-determined structural damping parameter B_m as

$$F_{\text{material damping}} = B_m \dot{Y} \ . \tag{3.24}$$

For completeness, an aerodynamic damping parameter B_a can be included to model the free response as

$$F_{\text{aero damping}} = \begin{cases} B_a \dot{Y} \left| \dot{Y} \right| & , \ V = 0 \\ 0 & , \ V \neq 0 \end{cases} \tag{3.25}$$

3.2 Equations of Motion

Employing the linearized single degree of freedom harvester model leads to the dimensional equations of motion in Y

$$M_e\ddot{Y} + B_m\dot{Y} + KY = \frac{1}{2}\rho_a DHV^2 C_N(\alpha) \tag{3.26}$$

where the effective mass is

$$M_e = \left(M_t + \frac{33}{140}\eta_b L\right) \tag{3.27}$$

and V is the incident wind velocity, K is the linear beam stiffness, ρ_a is the density of air, D is the characteristic width of the tip body, and H is the into-page length of the body. The aerodynamic force is given as a polynomial of the angle of attack α, defined as

$$C_N = \sum_{j=1}^{m} A_j \left|\alpha\right|^j \operatorname{sgn}(\alpha) \tag{3.28}$$

where the angle of attack is

$$\alpha = \frac{\dot{Y}}{V} - \xi\frac{Y}{L} \tag{3.29}$$

The attached harvesting circuit is governed by

$$C_p\dot{v} + \frac{1}{R_l}v + \Gamma\dot{Y} = 0 \tag{3.30}$$

where v is the voltage across the load, Γ is the linear displacement-current coupling coefficient, R_l is the load resistance, and C_p is the piezoelectric patch capacitance.

The equations can be nondimensionalized as

$$\begin{aligned} &y'' + 2\zeta_m y' + y - \kappa\chi = 2\mu U^2 C_N(\alpha), \qquad \alpha = \frac{y'}{U} - \frac{D}{L}\xi y \\ &\chi' + \tau_c\chi + y' = 0 \end{aligned} \tag{3.31}$$

with the definitions for dimensionless groups (note that y is scaled by D, not L)

$$\begin{gathered}
(\ )' = \frac{\mathrm{d}}{\mathrm{d}\tau}[\ ], \qquad y = \frac{Y}{D}, \qquad \chi = \frac{vC_p}{\Gamma}, \qquad \tau = \omega t, \qquad \kappa = \frac{\Gamma^2}{KC_p}, \\
\zeta_m = \frac{B_m}{2M_e\omega}, \qquad \mu = \frac{\rho_a D^2 H}{4M_e}, \qquad U = \frac{V}{\omega D}, \qquad \tau_c = \frac{1}{R_l C_p \omega}
\end{gathered} \tag{3.32}$$

where t represents time and $\omega = \sqrt{K/M_e}$ is the natural frequency of the oscillator at short circuit.

3.2.1 Approximate analytical solution

The approximate solution to Equation 3.31 is obtained using the method of multiple scales, an operation applicable to weakly nonlinear systems containing mechanisms which act on distinct time scales. A weak nonlinearity occurs when any nonlinear terms are scaled much smaller than the linear terms in an ODE. In the case of a galloping body, a "true" time scale describes the instantaneous position of the body while a slow time scale tracks the weakly nonlinear evolution of oscillation amplitude.

The scaling is accomplished using an arbitrarily small bookkeeping parameter ϵ such that "true" time is $T_0 = \tau$ and "slow" time is $T_1 = \epsilon\tau$. For the present problem, higher orders of ϵ (even slower time scales) can be neglected. The derivative operator is adapted such that

$$\frac{\mathrm{d}}{\mathrm{d}\tau} = D_0 + \epsilon D_1 + \mathcal{O}(\epsilon^2), \qquad \frac{\mathrm{d}^2}{\mathrm{d}\tau^2} = D_0^2 + 2\epsilon D_0 D_1 + \mathcal{O}(\epsilon^2). \tag{3.33}$$

where

$$D_0 = \frac{\mathrm{d}}{\mathrm{d}T_0}, \qquad D_1 = \frac{\mathrm{d}}{\mathrm{d}T_1}. \tag{3.34}$$

Additionally, two time scales admit zeroth and first order solutions for y and χ.

$$\begin{aligned} y(\tau) &= y_0(T_0, T_1) + \epsilon y_1(T_0, T_1) + \mathcal{O}(\epsilon^2) \\ \chi(\tau) &= \chi_0(T_0, T_1) + \epsilon \chi_1(T_0, T_1) + \mathcal{O}(\epsilon^2) \end{aligned} \tag{3.35}$$

It can be reasoned that the mechanism of amplitude growth occurs slowly because the energy input to the system is on the order of the energy dissipated—in the context of underdamped vibrations, energy dissipation must be small (controlled by ζ_m and κ), so a small net energy input requires small input flow energy (controlled by μ). Therefore, the appropriate parameters are scaled by ϵ.

$$\mu = \epsilon\mu, \qquad \zeta_m = \epsilon\zeta_m, \qquad \kappa = \epsilon\kappa \tag{3.36}$$

When Equations 3.33, 3.35, and 3.36 are substituted in to Equation 3.31, the resulting system can be divided by collecting the zeroth and first power of ϵ.

For ϵ^0:

The zeroth order system

$$\begin{aligned} D_0^2 y_0 + y_0 &= 0 \\ D_0\chi_0 + \tau_c\chi_0 &= -D_0 y_0 \end{aligned} \tag{3.37}$$

admits a zeroth order solution

$$\begin{aligned} y_0 &= a(T_1)\cos(T_0 + \beta(T_1)) \\ \chi_0 &= \frac{a(T_1)}{\sqrt{1+\tau_c^2}} \sin\left(T_0 + \beta(T_1) - \sin^{-1}\left(\frac{1}{\sqrt{1+\tau_c^2}}\right)\right) \end{aligned} \tag{3.38}$$

where a is the amplitude of oscillation and β is a phase shift function.

For ϵ^1:

Because both a and β are present in the expression for y_0, the solution can be determined

without consideration of higher-order equations in χ. The first order terms for y are as follows:

$$D_1^2 y_1 + y_1 = -2D_0 D_1 y_0 - 2\zeta_m D_0 y_0 + \kappa\chi_0 + 2\mu U^2 C_N(\alpha_0) \tag{3.39}$$

Let $\phi = T_0 + \beta$, $\gamma = 1/\sqrt{1+\tau_c^2}$, and $\psi = \sin^{-1}\gamma$. Substituting the zeroth order solutions, as well as the expression for C_N from Equation 2.6:

$$\begin{aligned} D_1^2 y_1 + y_1 =& 2D_1 a \sin\phi + 2aD_1\beta\cos\phi + 2\zeta_m a\sin\phi \\ &+ a\kappa\gamma\sin(\phi-\psi) \\ &+ 2\mu U^2 \sum_{\substack{j=1 \\ \text{odd}}}^{n} A_j (\alpha_0)^j + 2\mu U^2 \sum_{\substack{j=1 \\ \text{even}}}^{n} A_j |\alpha_0|^j \operatorname{sgn}(\alpha_0) \end{aligned} \tag{3.40}$$

Because the physical system does not have oscillations which grow to infinity, the "forcing" terms on the right hand side of Equation 3.40 must not resonate with y_1. This condition is enforced by ensuring the right hand side is orthogonal to both $\sin\phi$ and $\cos\phi$ throughout one cycle.

Before attempting integration of the right hand side of Equation 3.40, it is necessary to properly handle the $\operatorname{sgn}(\alpha_0)$ function. If the points at which α_0 changes sign are known, then the integral from 0 to 2π may be integrated across a number of smaller intervals within which the sign of α_0 does not change.

Rewriting Equation 3.29 using the above expressions for y,

$$\alpha_0 = -\frac{a}{U}\sqrt{\left(\frac{D}{L}\xi\right)^2 + 1}\ \sin\left(\phi + \tan^{-1}\left(\frac{D}{L}U\xi\right)\right) \tag{3.41}$$

it becomes clear that α_0 changes sign at

$$\phi = k\pi - \tan^{-1}\left(\frac{D}{L}U\xi\right), \qquad k \in \mathcal{Z} \tag{3.42}$$

Therefore, the integration of the even-order terms will change sign at $\phi = k\pi - \tan^{-1}\left(\frac{D}{L}U\xi\right)$ where k is an integer.

For orthogonality with $\cos\phi$,

$$\begin{aligned}
0 = &\int_0^{2\pi} \left[2D_1 a\sin\phi + 2aD_1\beta\cos\phi - 2\zeta_m a\sin\phi\right]\cos\phi\,\mathrm{d}\phi \\
&- \int_0^{2\pi} a\kappa\gamma\sin\left(\phi - \sin^{-1}(\gamma)\right)\cos\phi\,\mathrm{d}\phi \\
&+ 2\mu U^2\sum_{j=1}^{n} A_j\left(\frac{a}{U}\sqrt{\left(\frac{D}{L}\xi U\right)^2+1}\right)^j \\
&\quad\times\left\{-\int_0^{\pi-\tan^{-1}((D/L)\xi U)}\left[\sin\left(\phi+\tan^{-1}\left(\frac{D}{L}\xi U\right)\right)\right]^j\cos\phi\,\mathrm{d}\phi\right. \\
&\qquad+(-1)^j\int_{\pi-\tan^{-1}((D/L)\xi U)}^{2\pi-\tan^{-1}((D/L)\xi U)}\left[\sin\left(\phi+\tan^{-1}\left(\frac{D}{L}\xi U\right)\right)\right]^j\cos\phi\,\mathrm{d}\phi \\
&\qquad\left.-\int_{2\pi-\tan^{-1}((D/L)\xi U)}^{2\pi}\left[\sin\left(\phi+\tan^{-1}\left(\frac{D}{L}\xi U\right)\right)\right]^j\cos\phi\,\mathrm{d}\phi\right\}
\end{aligned} \tag{3.43}$$

gives a polynomial expression for $D_1\beta$ as

$$a\frac{\mathrm{d}\beta}{\mathrm{d}\tau} = \frac{\zeta_e}{\tau_c}a - 2\mu U^2\sum_{j=1}^{n} A_j\left(\frac{a}{U}\right)^j\left(\sqrt{\left(\frac{D}{L}\xi U\right)^2+1}\right)^{j-1} C_j \tag{3.44}$$

where ζ_e is electrical energy dissipation due to the harvesting circuit, defined as

$$\zeta_e = \frac{\tau_c\kappa}{2(1+\tau_c^2)} \tag{3.45}$$

and the coefficients can be expressed as a series function (derived by Bibo).

$$C_j = \frac{1-(-1)^j}{2^{j+2}}\left(\frac{(j+1)!}{\left(\left(\frac{1}{2}(j+1)\right)!\right)^2}\right) + \frac{1+(-1)^j}{2^j\pi}\sum_{k=0}^{j/2}\frac{(j+1)!\,(-1)^{\frac{1}{2}j-k}}{(j+1-k)!\,k!\,(j+1-2k)} \tag{3.46}$$

The amplitude equation proceeds from orthogonality with $\sin\phi$.

$$\begin{aligned}
0 = &\int_0^{2\pi} \left[2D_1 a\sin\phi + 2aD_1\beta\cos\phi - 2\zeta_m a\sin\phi\right]\sin\phi\,\mathrm{d}\phi \\
&- \int_0^{2\pi} a\kappa\gamma\sin\left(\phi - \sin^{-1}(\gamma)\right)\sin\phi\,\mathrm{d}\phi \\
&+ 2\mu U^2 \sum_{j=1}^{n} A_j \left(\frac{a}{U}\sqrt{\left(\frac{D}{L}\xi U\right)^2 + 1}\right)^j \\
&\quad\times\left\{ - \int_0^{\pi-\tan^{-1}((D/L)\xi U)} \left[\sin\left(\phi + \tan^{-1}\left(\frac{D}{L}\xi U\right)\right)\right]^j \sin\phi\,\mathrm{d}\phi \right. \\
&\qquad + (-1)^j \int_{\pi-\tan^{-1}((D/L)\xi U)}^{2\pi-\tan^{-1}((D/L)\xi U)} \left[\sin\left(\phi + \tan^{-1}\left(\frac{D}{L}\xi U\right)\right)\right]^j \sin\phi\,\mathrm{d}\phi \\
&\qquad\quad \left. - \int_{2\pi-\tan^{-1}((D/L)\xi U)}^{2\pi} \left[\sin\left(\phi + \tan^{-1}\left(\frac{D}{L}\xi U\right)\right)\right]^j \sin\phi\,\mathrm{d}\phi \right\}
\end{aligned} \tag{3.47}$$

giving

$$\frac{\mathrm{d}a}{\mathrm{d}\tau} = -(\zeta_e + \zeta_m)a + 2\mu U^2 \sum_{j=1}^{n} A_j \left(\frac{a}{U}\right)^j \left(\sqrt{\left(\frac{D}{L}\xi U\right)^2 + 1}\right)^{j-1} C_j\ . \tag{3.48}$$

At steady state, $\frac{\mathrm{d}\beta}{\mathrm{d}\tau} = \frac{\mathrm{d}a}{\mathrm{d}\tau} = 0$. Root-solving algorithms can then be used to solve Equations 3.44 and 3.48 and determine the steady phase shift and amplitude, respectively.

Output power

Once a solution for a has been obtained, the magnitude of the output power can be obtained using via the following electric power relationship:

$$\text{Power} = \text{Voltage} \times \text{Current}$$

Ohm's Law can be used to rewrite the power relationship as

$$P = \frac{v^2}{R_l}\ . \tag{3.49}$$

The load resistance can be moved to the left-hand side and the voltage v can be expressed in its dimensionless form to give:

$$PR_l = \chi^2 \left(\frac{\Gamma}{C_p} \right)^2 . \tag{3.50}$$

After moving the parenthetical group to the left, both sides of the equation are dimensionless.

$$PR_l \left(\frac{C_p}{\Gamma} \right)^2 = \chi^2 \tag{3.51}$$

An expression for dimensionless power could be obtained from either side of the equation as written above, but further simplification is possible. Because χ is a periodic waveform possessing a phase and an amplitude, the instantaneous power can be described with the same characteristics. Furthermore, it is often useful to simply express the amplitude of the power in terms of the physical displacement. Substituting the amplitude of χ into the above expression, let the definition for dimensionless power P^* follow as

$$P^* = |P| R_l \left(\frac{C_p}{\Gamma} \right)^2 = \frac{a^2}{1 + \left(\frac{1}{R_l C_p \omega} \right)^2} \tag{3.52}$$

For a given harvester system, the dimensionless output power rises with the square of the amplitude a. As shown in Equation 3.48 and the derivation thereof, a is dependent on R_l, C_p, and ω (among other parameters). These parameters can be optimized to maximize P^*. Both Bibo and Barrero *et al.* identify some optimum parameters for the linear system for small oscillation amplitudes, using very simple expressions for the aerodynamic coefficient C_N [51, 62]. For medium to large oscillation amplitudes, proper expression of C_N requires higher-order polynomials which do not permit analytical resolution of a. Therefore, optimizing P^* in such scenarios requires numerical routines.

While a numerical optimization is necessary for optimizing the mechanical and electrical

parameters, another parameter set remains to be optimized: aerodynamic parameters. If the magnitude of a is increased by modifying the geometry of the bluff body, and all other system parameters remain constant, then the dimensionless power will increase by necessity.

3.2.2 Universal approximation

Assuming the behavior of the body aerodynamics follow the quasi-steady assumption, the "universal" curve as developed by Novak [63] and extended by Bibo [51] can be adapted for the present system. The universal curve provides a framework for comparing harvester performance between implementations that use different bluff bodies, providing a reference performance criterion as a function of a reduced wind speed parameter. The curve is "universal" in the sense that the given performance criterion is independent of any mechanical or electrical parameters; the performance can be described purely in terms of its aerodynamic behavior, *i.e.* a solution universal for all systems with the same bluff body.

To establish a universal curve for the current system which accounts for the rotation of the bluff body, define $\hat{\alpha}$ such that

$$\hat{\alpha} = \frac{a}{U}\sqrt{\left(\frac{D}{L}\xi U\right)^2 + 1} \tag{3.53}$$

where $\hat{\alpha}$ is the magnitude of the apparent angle of attack.

Using $\hat{\alpha}$ as the aforementioned performance criterion, Equation 3.48 can be rewritten using $\hat{\alpha}$ to give

$$\frac{1}{U^*}\frac{\mathrm{d}\hat{\alpha}}{\mathrm{d}\tau^*} = -\frac{1}{U^*}\hat{\alpha} + 2\sum_{j=1}^{n} A_j \hat{\alpha}^j C_j \ . \tag{3.54}$$

where

$$U^* = \frac{U\mu}{\zeta_m + \zeta_e}, \qquad \tau^* = (\zeta_m + \zeta_e)\tau \ . \tag{3.55}$$

When $\xi = 0$, as in the case of pure translation, the equation of the universal curve reduces to

that used by Bibo.

Framing the problem in terms of $\hat{\alpha}$ reduces the modulation equation to dependence on only two independent variables: U^* and τ^*. For steady-state problems, $\frac{\mathrm{d}\hat{\alpha}}{\mathrm{d}\tau^*} = 0$. The roots of $\hat{\alpha}$ are only dependent on U^*, a twice-reduced wind speed parameter, and the C_N curve for the body. Therefore, any system employing the same bluff body will share the same curve of $\hat{\alpha}$ vs. U^*. As such, the universal formulation is a powerful tool for directly comparing the relative power production capability of different GFEH bluff body configurations.

As previously discussed, the accuracy of low-order aerodynamic polynomials is questionable but might be sufficient in scenarios where accuracy is only needed over a small angle range (such as high damping designs). If the aerodynamic data can be accurately captured by a 9^{th}-order odd polynomial, the steady-state equation can be written as

$$0 = -\frac{1}{2U^*}\hat{\alpha} + A_1C_1\hat{\alpha} + A_3C_3\hat{\alpha}^3 + A_5C_5\hat{\alpha}^5 + A_7C_7\hat{\alpha}^7 + A_9C_9\hat{\alpha}^9 \ .$$

When the trivial root is eliminated, the expression can be expanded in terms of $Z = \hat{\alpha}^2$ to give

$$0 = -\frac{1}{2U^*} + A_1C_1 + A_3C_3Z + A_5C_5Z^2 + A_7C_7Z^3 + A_9C_9Z^4 \ .$$

As a 4^{th}-order polynomial, the solutions for Z can be resolved analytically (See [64] for solution procedure).

The transient equations are also analytically solvable when the aerodynamics are captured by a 7^{th}-order odd polynomial. The formulas will be listed here for convenience. First, expand the modulation equation in terms of $Z = \hat{\alpha}^2$ and rearrange.

$$\frac{1}{\frac{35}{32}A_7U^*}\frac{\mathrm{d}Z}{\mathrm{d}\tau^*} = Z\left[Z^3 + \frac{\frac{5}{4}A_5}{\frac{35}{32}A_7}Z^2 + \frac{\frac{3}{2}A_3}{\frac{35}{32}A_7}Z + \frac{2\left(A_1 - \frac{1}{U^*}\right)}{\frac{35}{32}A_7}\right] \tag{3.56}$$

To abbreviate the notation, the following parameter groups will be used:

$$C_3 = \frac{35}{32}A_7U^*, \qquad C_0 = \frac{2\left(A_1 - \frac{1}{U^*}\right)}{\frac{35}{32}A_7}, \qquad C_1 = \frac{\frac{3}{2}A_3}{\frac{35}{32}A_7}, \qquad C_2 = \frac{\frac{5}{4}A_5}{\frac{35}{32}A_7} \tag{3.57}$$

The cubic solution procedure depends on three groups of the new coefficients.

$$\Delta_0 = C_2^2 - 3C_1, \qquad \Delta_1 = 2C_2^3 - 9C_2C_1 + 27C_0, \qquad S = \left[\frac{1}{2}\left(\Delta_1 + \sqrt{\Delta_1^2 - 4\Delta_0^3}\right)\right]^{1/3} \tag{3.58}$$

The three non-trivial roots of Z are given for $k = 1, 2, 3$.

$$Z_k = -\frac{1}{3}\left(C_2 + \left(-\frac{1}{2} + \frac{\sqrt{3}}{2}\,\mathbf{i}\right)^k S + \frac{\Delta_0}{\left(-\frac{1}{2} + \frac{\sqrt{3}}{2}\,\mathbf{i}\right)^k S}\right) \tag{3.59}$$

Rearranging into integral form,

$$C_3 \int \mathrm{d}\tau^* = \int \frac{\mathrm{d}Z}{Z(Z - Z_1)(Z - Z_2)(Z - Z_3)} \tag{3.60}$$

Carrying out the integration from some initial condition $Z_i > 0$, the dimensionless time τ^* to reach a given Z can be determined.

$$C_3\tau^* = \frac{\ln\left(\frac{Z - Z_1}{Z_i - Z_1}\right)}{Z_1(Z_1 - Z_2)(Z_1 - Z_3)} + \frac{\ln\left(\frac{Z - Z_2}{Z_i - Z_2}\right)}{Z_2(Z_2 - Z_1)(Z_2 - Z_3)} + \frac{\ln\left(\frac{Z - Z_3}{Z_i - Z_3}\right)}{Z_3(Z_3 - Z_1)(Z_3 - Z_2)} + \frac{\ln\left(\frac{Z_i}{Z}\right)}{Z_1Z_2Z_3} \tag{3.61}$$

The universal transient solution can be visualized as a surface in $U^* \times \tau^* \times Z$ space. When a 7^{th}-order odd polynomial is sufficient to model the aerodynamics of a GFEH, the universal curve permits comparison of transient as well as steady-state performance.

3.3 Model Stability

The beauty of the method of multiple scales lies in the modulation equations. Both the value and the stability of the amplitude of oscillation can be directly drawn from the modulation equations. The stability is determined through a linear analysis of the fixed points of $\hat{\alpha}$. To this end, the Jacobian of the modulation equations can be written as

$$J = \frac{\partial}{\partial \hat{\alpha}} \left[\frac{1}{U^*} \frac{\mathrm{d}\hat{\alpha}}{\mathrm{d}\tau^*} \right]_{fp} = -\frac{1}{U^*} + A_1 + 2 \sum_{j=2}^{n} j A_j \hat{\alpha}_{fp}^{j-1} C_j \tag{3.62}$$

where $\hat{\alpha}_{fp}$ is a fixed point of the modulation equations. For $\hat{\alpha}_{fp}$ to be stable, the eigenvalues of the associated Jacobian matrix must all have negative real parts.

The immediately obvious result deduced from Equation 3.62 is that the trivial fixed point $\hat{\alpha}_{fp} = 0$ loses stability when

$$U^* > \frac{1}{A_1} \tag{3.63}$$

which marks the cut-in wind speed at which the system begins self-excited oscillations.

When the remaining fixed points are evaluated, a bifurcation diagram such as that in Figure 3.6 can be produced. At the cut-in wind speed, a supercritical Hopf bifurcation (SHB) splits the trivial fixed point into an unstable zero fixed point and a branch of stable oscillations whose magnitude increases rapidly with U^*. A cyclic fold bifurcation (CFB) leads to a brief interlude of instability after which the stable branch resumes through another CFB.

The unstable region is evidence of a body with hysteretic behavior and has a direct physical link to the aerodynamics of the bluff body: it is present if there is an inflection point in the polynomial representation of C_N [33, 65, 66]. Figure 3.7 is an example bifurcation diagram. Imagine that the diagram is a stationary surface pierced by a vertical column uniquely located on the horizontal plane by U^* and the instantaneous $\hat{\alpha}$ of the system is

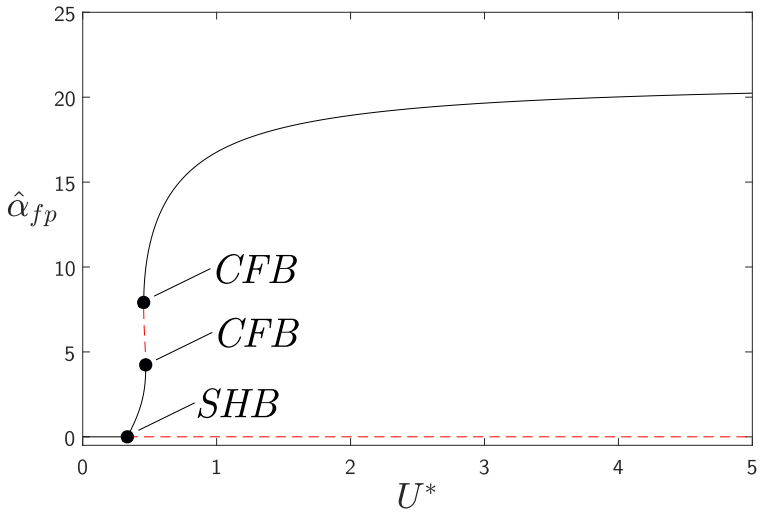

Figure 3.6: The bifurcation diagram for the square body.

represented by an ant crawling on the column (the starting point of the ant is the initial condition of the system). If the column only intersects the surface in one point, then the ant will always crawl toward the value of $\hat{\alpha}$ at the intersection point; whether the ant starts above or below the surface is immaterial. If the column intersects the surface within the unstable region, there are three points of intersection: an unstable intersection with stable intersections above and below it. If the ant starts crawling from the bottom or the top of the column, he will stop at the first stable intersection he encounters. However, if the ant starts somewhere in between a stable intersection and an unstable intersection, the ant will crawl toward the stable intersection.

The nonzero fixed points can be estimated using some physical intuition of the dynamical system. In highly-damped systems, a steady state is reached when the damping balances out the energy pumped into the system by the galloping phenomenon each cycle. However, lightly-damped systems tend to be self-limited by the aerodynamic force. As was demonstrated in Figure 2.4, the first nonzero root of the C_N curve, α_0, flips the sign of the force on the tip body and the fluid itself begins to remove energy from the system. The steady-state will be obtained when the fluid removes the energy it adds each cycle. Therefore, as a first

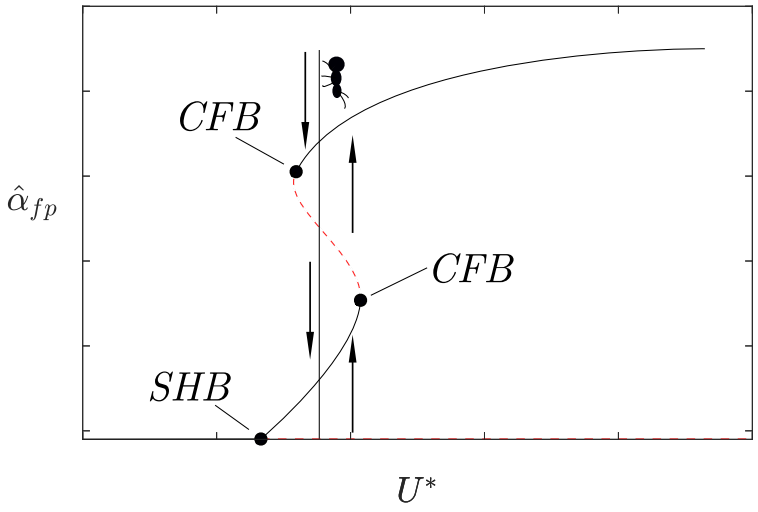

Figure 3.7: An example bifurcation diagram to demonstrate hysteretic behavior.

approximation, the steady state value of $\hat{\alpha}_{fp}$ will tend to be near α_0 for high enough U^*. For comparison with Figure 3.6, α_0 for the square body is approximately 18°.

3.4 Influence of ξ

The model developed and applied by Bibo *et al.* on the present system is not fundamentally changed by the inclusion of a linear rotation parameter ξ. The natural question arises: does ξ substantially influence the models developed for energy harvesters?

First, consider the error introduced into α by setting $\xi = 0$. It is not uncommon to have deflections up to $\frac{Y}{L} \approx 0.3$ at which point the tip has already rotated 25°! Failing to include the tip rotation causes severe misjudgments of the aerodynamic force experienced by the body.

Second, consider that the universal model predicts that any given body geometry will lead to a single equation for $\hat{\alpha}$. Although a given body geometry will produce a solution for

$\hat{\alpha}$ independent of ξ, the value of a depends on U, D, L, and ξ:

$$a = \frac{\hat{\alpha}U}{\sqrt{1 + \left(\frac{D}{L}U\xi\right)^2}}$$

Substituting the above expression for a into Equation 3.52, the dependence of the dimensionless output power on ξ becomes plain.

$$P^* = \frac{(\hat{\alpha}U)^2}{\left(1 + \left(\frac{D}{L}U\xi\right)^2\right)\left(1 + \left(\frac{1}{R_l C_p \omega}\right)^2\right)}$$

Compare the percent error in the power predicted for a given $\hat{\alpha}$ without ξ ($P^*_{\xi=0}$) to that found when using ξ (P^*). Let the percent error be defined as

$$\% \text{ Error} = \frac{P^*_{\xi=0} - P^*}{P^*} = \frac{P^*_{\xi=0}}{P^*} - 1 \ . \tag{3.64}$$

Both $P^*_{\xi=0}$ and P^* contain the following group of parameters:

$$\frac{(\hat{\alpha}U)^2}{\left(1 + \left(\frac{1}{R_l C_p \omega}\right)^2\right)}$$

After canceling the above group of parameters from both terms, the percent error simplifies to

$$\% \text{ Error} = \left(\frac{D}{L}U\xi\right)^2 = \left(\frac{V}{\omega L}\xi\right)^2 \tag{3.65}$$

It is clear that failure to include ξ will always over-predict the output power. To highlight the significance of the error, the percent error was plotted over a range of length-reduced wind speed in Figure 3.8.

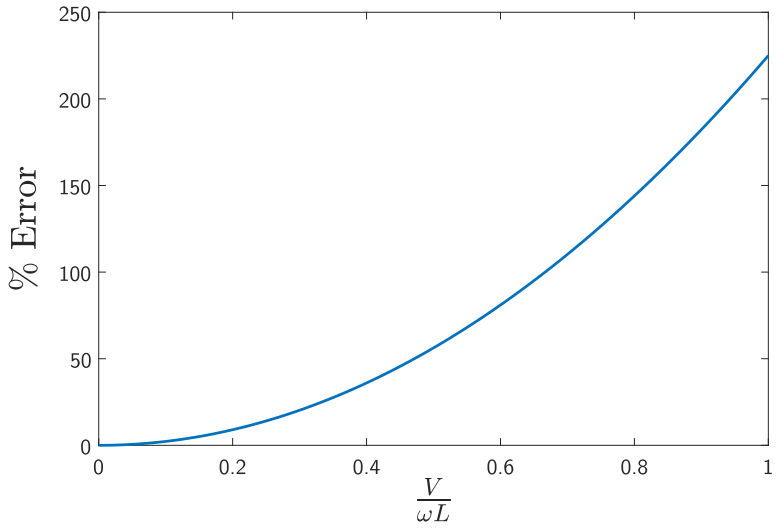

Figure 3.8: The percent error introduced in the dimensionless power output when ξ is neglected.

3.5 Summary

Analytical nonlinear analysis and nonlinear solutions were used to establish that the tip rotation of an Euler-Bernoulli beam can be predicted with good accuracy using a constant $\xi = 1.5$ for small to moderate deformations, despite the traditional limitations of small angle assumptions. Therefore, the weakly nonlinear system was adopted for the present work. The method of multiple scales was applied to Equation 3.31 to produce an approximate analytical solution accounting for the kinematic effects of tip rotation, Equation 3.48. The approximate solution was used to calculate the cut-in wind speed required to incite vibrations from rest in Equation 3.63.

The significance of including ξ in the model was highlighted by examining its effect on the calculation of the output power. The error introduced by neglecting ξ is significant even at low values of reduced wind speed; how then has the standard model been used with good convergence in previous studies? Why have the models not all dramatically over-predicted the output power? It may be that failing to consider the tip rotation has been "canceled out" by also neglecting the *aerodynamic* effects of tip rotation, which will be examined

experimentally in the next chapter.

Chapter 4

Model Evaluation

The quasi-steady model proposed in Chapter 3 was evaluated using experimental trials conducted in a laboratory environment. After discussing the experimental methodology, this chapter expands the results of the procedures into two sections: one for the square body and one for the trapezoidal body. Finally, the chapter closes with the main conclusions of the present experimental work.

4.1 Experimental Setup and Procedure

4.1.1 Setup

All test systems were placed in an Aerolab Educational Wind Tunnel, which has a 12 in or 305 mm square test chamber cross section, as shown in Figure 4.1. An Omega vane-type anemometer was used to calibrate the tunnel's wind speed control to within $\pm 0.05\,{}^{\mathrm{m}}/_{\mathrm{s}}$.

A Micro-Epsilon optoNCDT 1302 laser vibrometer was used to measure the amplitude and frequency of the tip displacement. Parallax error was addressed as documented in Appendix A. Because the model evaluation procedure requires a large number of trials in different configurations, non-contact displacement measurement was selected as the best comparative

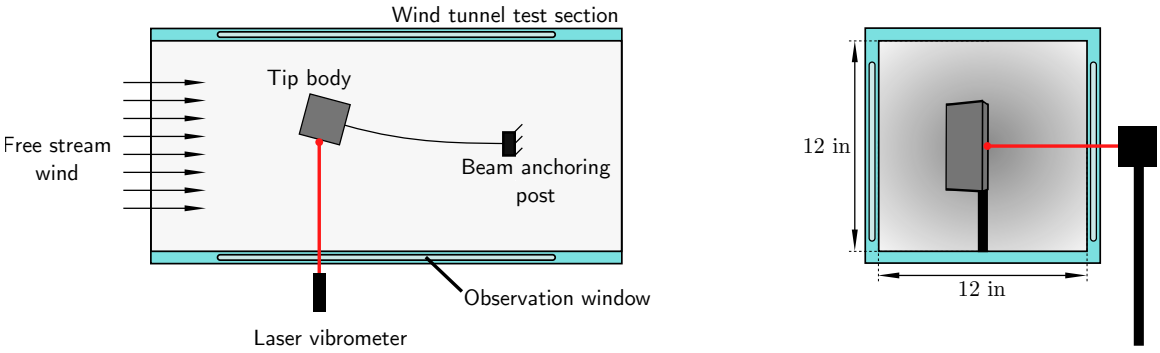

Figure 4.1: Schematic of the experimental system layout.

Beam No.	L_b (m)	W_b (m)	t_b (m)	Material	η_b $\left({}^{\text{kg}}/_{\text{m}}\right)$	E_b (GPa)
1	0.254	0.0317	0.0025	Aluminum	0.17	30.8
2	0.254	0.0158	0.0025	Aluminum	0.078	30.8
3	0.343	0.0317	0.0025	Aluminum	0.17	30.8
4	0.432	0.0317	0.0025	Aluminum	0.17	30.8
5	0.245	0.03	0.0008	Mild steel	0.15	200
6	0.245	0.03	0.0008	Stainless steel	0.18	200
7	0.285	0.03	0.0008	Stainless steel	0.18	200

Table 4.1: Beam configurations for experimental trials. Beam 5 was laminated with a piezoelectric strip at its base.

criterion, as Bibo has already validated the linear electrical damping contribution ζ_e of the harvesting circuit and established the displacement-power relationship given in Equation 3.52 [15]. Working in terms of displacement avoids the cost and repeatability challenges of supplying and positioning new piezoelectric patches for each beam configuration. The collection of beams and the numbered configurations are documented in Table 4.1.

The bluff bodies used in all trials are based around a square profile or a trapezoidal profile with the proportions shown in Figure 4.2 and the dimensions provided in Table 4.2. The bluff bodies were mounted on the beam such that the tip of the beam was embedded into the center of the bluff body.

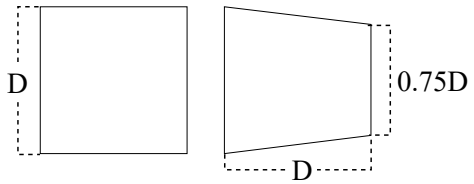

Figure 4.2: The proportions of the square (left) and the trapezoidal (right) bluff bodies.

Body	Square	Trapezoid
Mass (kg)	0.0451	0.0370
D (m)	0.0254	0.0254
H (m)	$5.75D$	$5.75D$

Table 4.2: Dimensions of bluff bodies.

4.1.2 Procedure

The experimental trials were started from rest, with no initial movement of the oscillator. The wind tunnel was rapidly ramped up to the desired wind velocity and the displacement response was measured at the tip of the beam. The time history data was passed through a Butterworth filter to smooth out noise and produce a waveform with time-varying amplitude as shown in Figure 4.3.

The amplitude of the waveform in Figure 4.3 can be scaled by D to determine a, which can then be used to find $\hat{\alpha}$ from Equation 3.53 or to find the output power using Equation 3.52.

The determination of the damping coefficient is critical to the analysis of the experimental data. This was accomplished by recording a time history of the free decay of the system from an initial condition similar in magnitude to the steady state oscillation of the system.

If a quadratic air damping term $\zeta_a|\dot{y}|\dot{y}$ is passed through the method of multiple scales, the modulation equation for the amplitude of free decay becomes

$$\frac{\mathrm{d}a}{\mathrm{d}\tau} = -\zeta_m a - \frac{4}{3\pi}\zeta_a a^2. \tag{4.1}$$

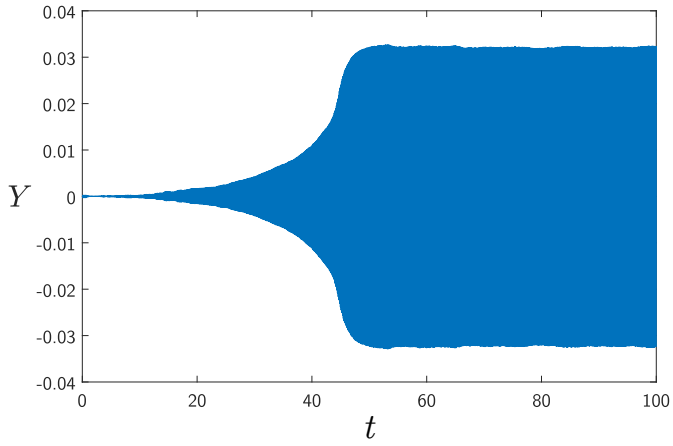

Figure 4.3: An example time history as measured by the vibrometer.

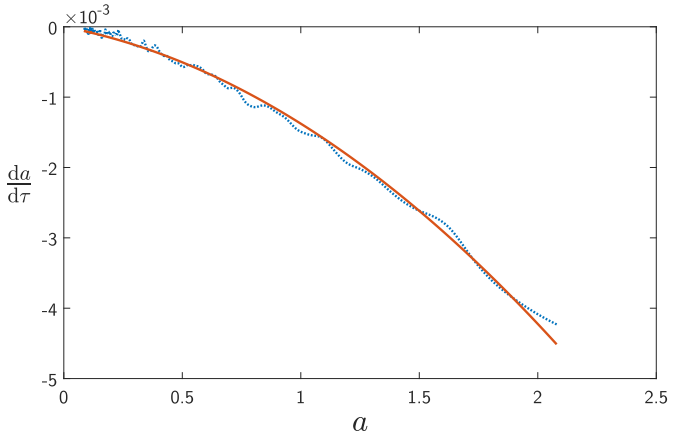

Figure 4.4: An example quadratic fitment used to find the damping coefficients.

The values of a and $\frac{\mathrm{d}a}{\mathrm{d}\tau}$ were extracted from the data and a quadratic curve fit was used to find ζ_m and ζ_a as shown in Figure 4.4. As discussed in Section 3.1.4, the quadratic damping components are neglected: the vortex shedding responsible for the aerodynamic viscous damping only occurs in still air.

"Steady state" data is taken once the system response has reached a plateau, as seen after 50 seconds in Figure 4.3. "Transient" data encompasses the amplitude growth period from 0–50 seconds in this example. It is important to make the distinction that "transient" refers to the amplitude growth of the body and not the wind condition, as the wind condition is

considered steady.

4.2 Square Body

4.2.1 Steady State Amplitude

The first step in evaluating the model is to pick a single bluff body and examine whether the analytical approximation for amplitude can predict the steady-state oscillation amplitude of the system. The square body is selected as the initial test case due to its ubiquity in literature, possessing the following quasi-steady aerodynamic coefficients:

$$\begin{aligned} A_1 &= 3 & A_7 &= 34312.317 \\ A_2 &= -39.861 & A_8 &= -26226.065 \\ A_3 &= 626.7 & A_9 &= 12369.416 \\ A_4 &= -4299.43 & A_{10} &= -3292.734 \\ A_5 &= 14545.766 & A_{11} &= 378.995 \\ A_6 &= -28379.839 \end{aligned} \tag{4.2}$$

The results for the steady state angle of attack are presented in Figure 4.5. Note that the true cut-in wind speed is notoriously hard to determine for systems with very low damping coefficients, so the initial U^* of each data set should not be interpreted as such [10]. Loosely speaking, however, it can be observed that the data sets might tend to target a cut-in in the area of 0.3–0.6, similar to the quasi-steady prediction.

The "universal" solution provided in Equation 3.54 would predict that all data points would coincide with the solid blue line. Clearly, however, the model is insufficient to describe the performance of the physical system, and $\hat{\alpha}$ is dependent on more model parameters than simply U^* due to the affect of body rotation. The missing parameter will be investigated using analysis of the transient growth of the amplitude.

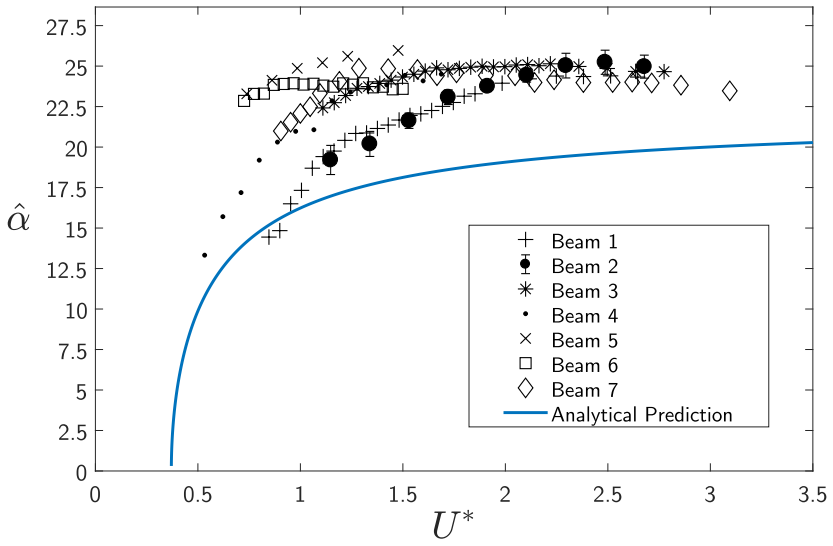

Figure 4.5: Steady state amplitude results for the square body. The error bars on the data for Beam 2 indicate the spread of data when repeated 10 times.

4.2.2 Growth Analysis

Based on the existing knowledge of bluff body aerodynamics, it can be expected that the square body would be strongly influenced by flow curvature due to the closeness of the afterbody to the shear layers in the surrounding flow. As discussed in Section 2.3, the effects of flow curvature are often categorized as a function of a parameter k, the inverse of U. If curvature effects change the aerodynamic forces on the body as a function of U, then there is no single set of aerodynamic coefficients that can generate a universal solution and Equation 3.54 breaks down.

Unsteady aerodynamics typically involve explicit time dependent terms to consider forces which decay into steady-state values. Even steady-state vortex shedding is a time-dependent phenomena. Attempting to model the exact time-dependent influence of the rotation of the bluff body would require numerical fluid-structure interaction simulation. To the author's knowledge, there is not yet a useful closed-form approximation of such a phenomenon.

However, the phenomenon of galloping is not time-explicit, as it acts as a function of

the body motion. Similarly, the phenomenon of dynamic stall can be described in terms of the motion of the airfoil without explicit time scales. As the body periodically rotates through its path, the curvature affects must also fall into a pattern such that the net force experienced by the body can be stated as a function of position (or angle of attack) rather than time. In this way the influence of curvature might be interpreted through its *average* effect. The experimental results showed little to no influence of any explicit time-dependent influence, strengthening the idea that the curvature can be expressed through a new "effective" aerodynamic force curve

$$C_N(\alpha, U) = \sum_{j=1}^{n} A_j(U) \cdot |\alpha|^j \cdot \text{sgn}(\alpha) \tag{4.3}$$

where the coefficients A_j are functions of U.

Whereas the steady-state data gives one indicator of system response over a range of U or U^*, the build-up of oscillation amplitude provides insight into the system dynamics at a single U. The modulation equation derived from the method of multiple scales (Equation 3.48) provides a trajectory for the oscillation amplitude in terms of the aerodynamic coefficients A_j. Therefore, if the time history of the oscillation amplitude is known, then the modulation equation can be used "in reverse" to provide insight into the aerodynamic coefficients.

Two approaches will be used in the transient growth analysis: Slice-by-Slice and Aggregate methods.

Slice-by-Slice

When the aerodynamic coefficients are taken as functions of U, the growth rate of a can be viewed as a function of two variables: U and a. Each experimental trial at a constant U is treated as one "slice" of a larger cloud of data in the $U \times a \times \frac{\mathrm{d}a}{\mathrm{d}\tau}$ space. This slice can be fitted with a polynomial function of a matching the form of Equation 3.48. The transient

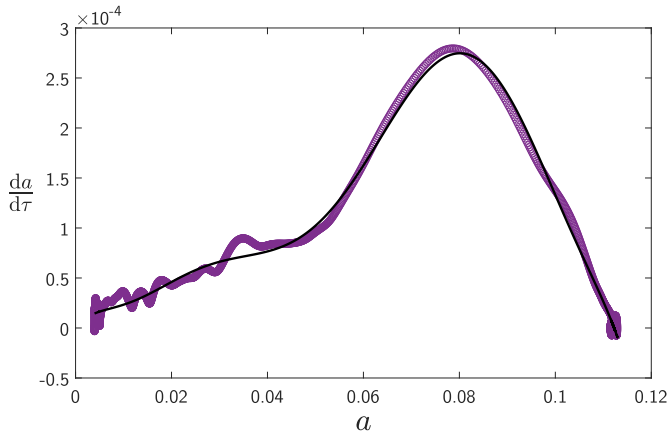

Figure 4.6: An example 9$^{\text{th}}$-order fitment used to find the effective aerodynamic coefficients. The thin line is the polynomial fit.

growth of the amplitude always followed some sort of polynomial trajectory, validating the presumption of an effective or averaged aerodynamic force curve.

When the procedure was applied to all of the tested data, the slices could be combined into a single 3D plot. A clear evolution in aerodynamic behavior emerged, as shown in Figure 4.7, a 3D plot of Equation 4.3. The slope at $\alpha = 0$, A_1, varies little with U, so the cut-in U^* is expected to remain roughly the same, as hinted at during the initial inspection of the steady-state results. Although there is a strong peak in C_N at low values of U, the aerodynamic curves begin to decay into the quasi-steady curve as U increases. The effect of the flow curvature does not completely disappear in the present data set, though, as the rotation results in galloping over a much broader range of α_0.

The features of the surface in Figure 4.7 can be broken into the zero crossings in Figure 4.8 and the peak C_N values in Figure 4.10. Figure 4.8 shows that α_0 is initially below the quasi-steady value for low U and increases with U. It is known that increasing the Reynolds number tends to increase the angles of flow reattachment and shifts the force polynomial to higher α [2], but the scatter in Figure 4.9 suggests that the effect is not primarily due to the changing Reynolds number.

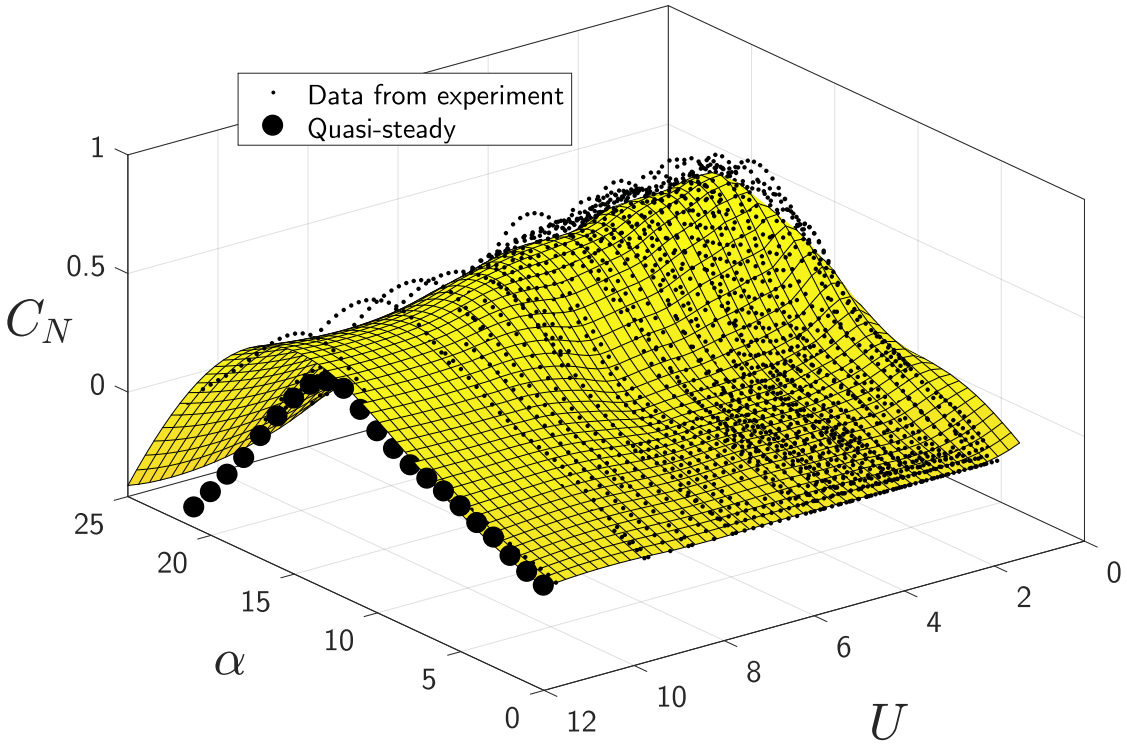

Figure 4.7: A LOWESS surface interpolation of the effective aerodynamic polynomials for each growth time history recorded. $R^2 = 0.93$.

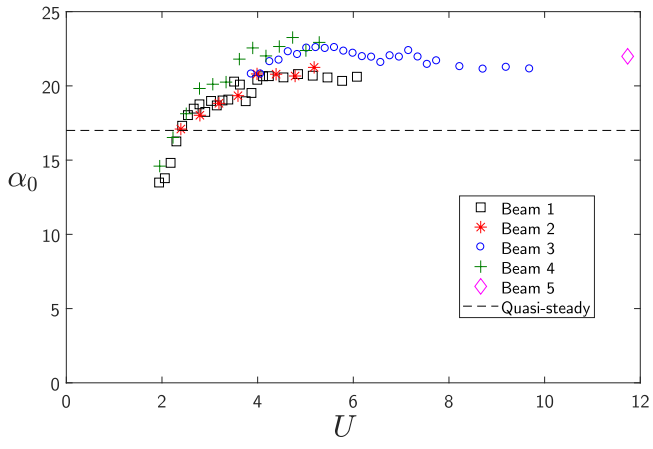

Figure 4.8: The roots of the aerodynamic polynomial α_0 as a function of U.

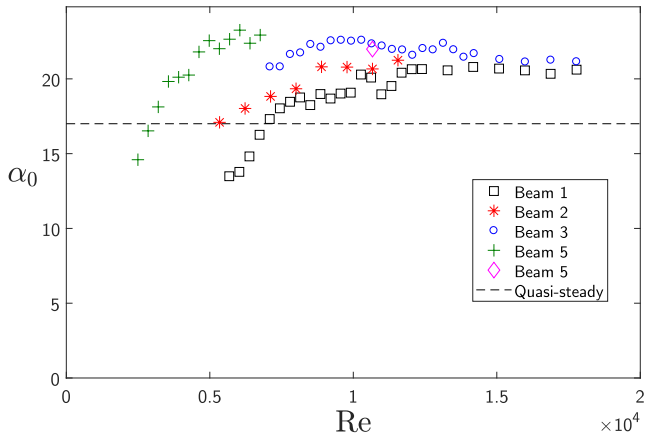

Figure 4.9: The roots of the aerodynamic polynomial α_0 as a function of the Reynolds number.

Recalling the expression of C_N as

$$C_N = C_L \cos\alpha - C_D \sin\alpha$$

it becomes apparent that at higher α, the drag component has increasing influence. As shown in Figure 2.12, rotation of the body induces roll-up of a vortex behind the body, decreasing the base pressure and increasing the drag force. The likely physical explanation for the dip below the quasi-steady α_0 is that the strong curvature at low U creates a large drag component that takes over at smaller α and forces C_N to zero.

Recall that the universal solution indicates that as $\zeta_m \to 0$, $U^* \to \infty$, and $\hat{\alpha}$ eventually reaches a plateau slightly beyond α_0. In other words, ζ_m can be manipulated so that the system can achieve the same $\hat{\alpha}$ for any U. The significance of Figure 4.8 is that U can influence the potential steady-state amplitude of the system independently from ζ_m. Therefore, U becomes a design parameter of interest.

The variation of the peak C_N with U is presented in Figure 4.10. There is a loosely grouped hump at low U followed by a steady decline to the quasi-steady peak value. Figure 4.10 displays the interplay between the lift and drag forces. At the lowest U, the strong drag

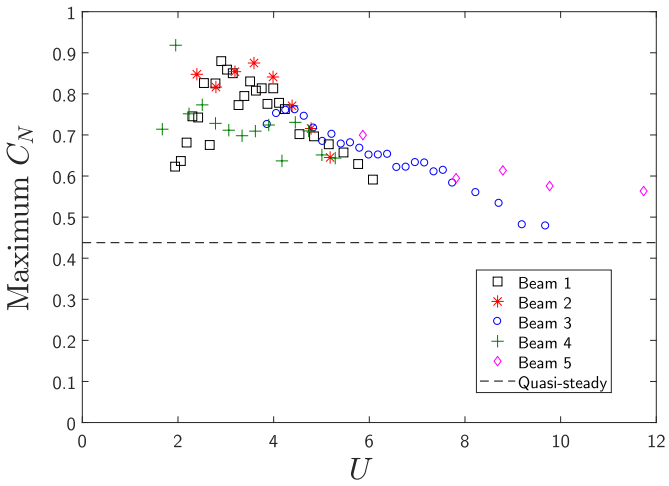

Figure 4.10: The peak lift coefficient.

reduces C_N greatly and C_N does not develop fully. Beyond the peak at which C_L and C_D are optimally balanced, the decreasing curvature causes a reduction in suction, lowering the peak C_N.

A precise model for capturing the U dependence of the aerodynamics has not yet been established, to the author's knowledge. However, a surface fit of the C_N data could potentially provide an improvement over the quasi-steady model as it stands.

The Slice-by-Slice method offers fast convergence on the fitments of the individual trials and provides a quick overview of general trends in the data. However, the discrete treatment of each experimental trial does not lend itself to generating a single useful function to supplement the quasi-steady data. Therefore, the Aggregate method will be applied.

Aggregate

The Slice-by-Slice method provided enough insight to suggest that, for a given body, C_N could be described by a single surface in α and U. It is of interest to identify such a "best-fit" surface using all the experimental data in one calculation. To this end, the universal equation can be rearranged to separate the aerodynamic parameters on the right-hand side and the

remaining harvester parameters on the left-hand side.

$$\frac{1}{U^*}\left[\frac{\mathrm{d}\hat{\alpha}}{\mathrm{d}\tau^*}+\hat{\alpha}\right]=2\sum_{j=1}^{n}A_j(U)\hat{\alpha}^jC_j \tag{4.4}$$

Let A_j take the assumed form

$$A_j=c_{1j}\mathrm{e}^{-c_{2j}U}+c_{3j}\mathrm{e}^{-c_{4j}U}+c_{5j}\mathrm{e}^{-c_{6j}U}+A_{j,\mathrm{qs}} \tag{4.5}$$

where $A_{j,\mathrm{qs}}$ is the quasi-steady aerodynamic coefficient value and c_{2j}, c_{4j}, and c_{6j} are positive. Because the experimental data provides a value for $\frac{1}{U^*}\frac{\mathrm{d}\hat{\alpha}}{\mathrm{d}\tau^*}$ and $\frac{\hat{\alpha}}{U^*}$ at every τ^* and U, the remaining free parameters, the c values, can be fitted using global optimization algorithms. An objective function F_{obj} over all N collected data points can be stated

$$F_{\mathrm{obj}}=\sum_{k=1}^{N}\left(\frac{1}{U_k^*}\left[\left.\frac{\mathrm{d}\hat{\alpha}}{\mathrm{d}\tau^*}\right|_k+\hat{\alpha}_k\right]-2\sum_{j=1}^{n}\left(c_{1j}\mathrm{e}^{-c_{2j}U_k}+c_{3j}\mathrm{e}^{-c_{4j}U_k}+c_{5j}\mathrm{e}^{-c_{6j}U_k}+A_{j,\mathrm{qs}}\right)\hat{\alpha}_k^jC_j\right)^2 \tag{4.6}$$

Differential evolution was adopted as an optimization algorithm to minimize the objective function using the freely available MATLAB code `deopt.m` [67]. Due to the intensive calculations required, the optimization was computed on the Palmetto Cluster. The resulting C_N surface after 20 000 iterations is given in Figure 4.11.

The "dip" in the top of the surface is not physically relevant and is the result of insufficient iterations of the optimization algorithm. However, the surface does provide significantly better prediction of the steady-state amplitude of the galloping system, as shown in Figure 4.12.

While refined optimization methods would improve the physical accuracy of this C_N surface, the potential usefulness of a C_N surface is apparent even with rudimentary fitting.

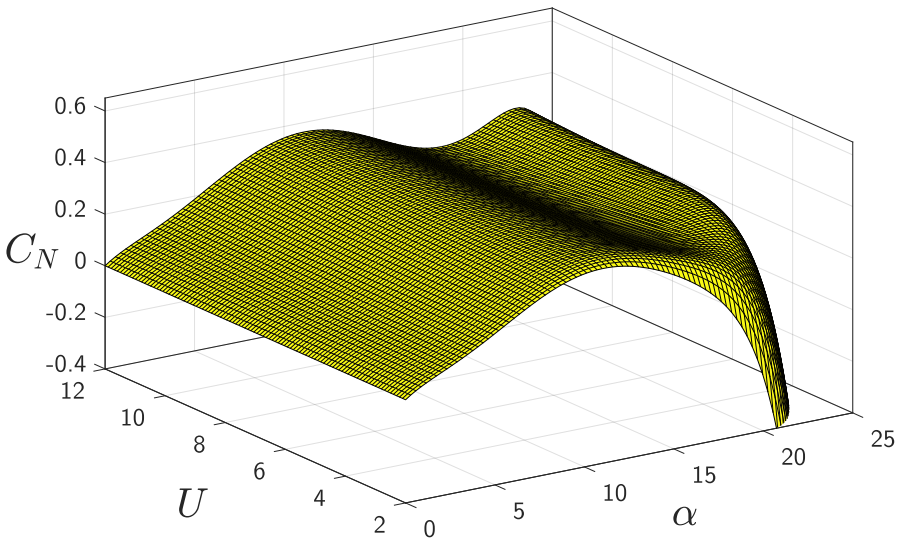

Figure 4.11: C_N surface found by minimizing Equation 4.6.

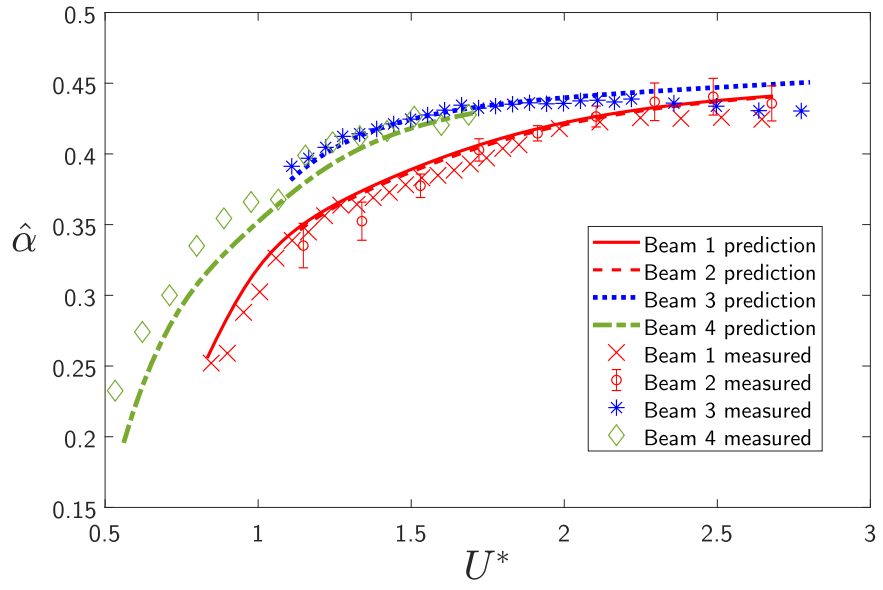

Figure 4.12: Steady state amplitude results for the square body. The error bars on the data for Beam 2 indicate the spread of data when repeated 10 times. Predictions made with C_N surface found by minimizing Equation 4.6 (shown in Figure 4.11).

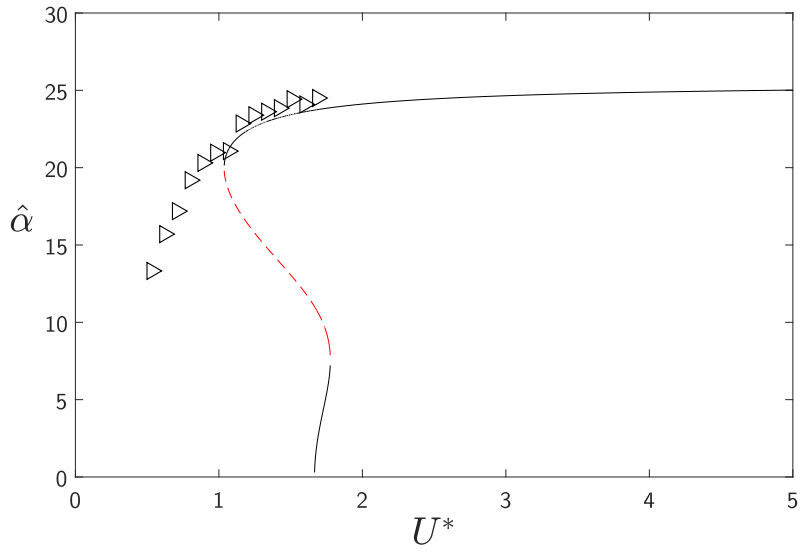

Figure 4.13: Steady state amplitude results for the trapezoidal body. The trials were conducted on Beam 1.

4.3 Trapezoidal Body

Just as the sensitivity of the square body to flow curvature might be expected due to its afterbody, it might also be expected that the trapezoidal profile would be less sensitive to curvature due to the taper in its afterbody. To briefly examine the validity of this expectation, steady state data was collected for the trapezoidal body on Beam 1. Beyond significant amplification at low U^*, the quasi-steady model *very* accurately predicts the response of the body with coefficients extrapolated from data from Luo (all even coefficients zero) [1]:

$$A_1 = 0.6, \qquad A_3 = -6, \qquad A_5 = 237, \qquad A_7 = -1300 \tag{4.7}$$

To further investigate the amplification at low U^*, the amplitude growth histories were analyzed using the Slice-by-Slice method and presented as an interpolation surface in Figure 4.14. As can be seen, the slope at $\alpha = 0$ is strongly amplified by the curvature of the flow, explaining how the beam-mounted model began galloping before the quasi-steady model predicted. Although the trapezoid was expected to be less sensitive to curvature than the

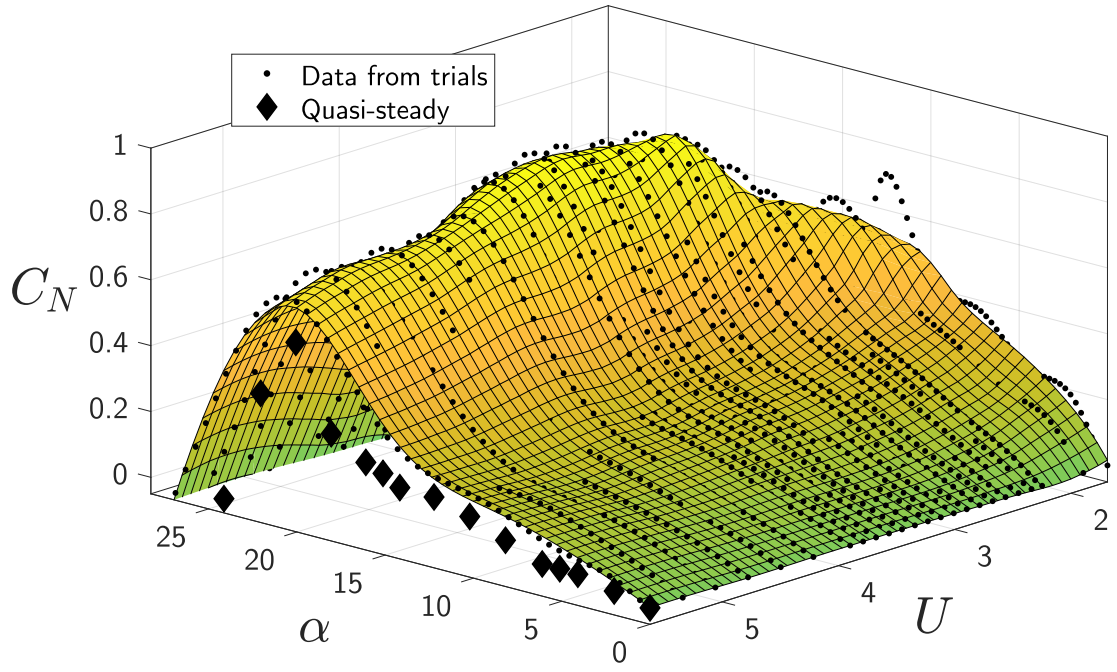

Figure 4.14: A LOWESS surface interpolation of the effective aerodynamic polynomials for each growth time history recorded for the trapezoid. $R^2 = 0.98$.

square, its tapered side faces may allow it to capitalize on strong vortices rolled up behind the body; on the square, the rolled up vortex is trapped by the rear face and contributes exclusively to drag, whereas the trapezoid might feel the vortex on its side face with both lift and drag components. Finally, because quasi-steady theory places the side faces very far from the shear layers, any curvature will offer large relative gains in suction because there was little at the start.

Just as in the square case, there is a boost in the peak C_N at low U. However, as U grows, the aerodynamic curves for the trapezoid do tend toward the quasi-steady case with much better convergence than the square body. In this sense, the trapezoid might be considered "less sensitive" to curvature.

4.4 Summary

The quasi-steady model fails to accurately predict the behavior of the square and trapezoidal bodies in galloping oscillation when mounted to a cantilever beam. The quasi-steady model under-predicts the amplitude of oscillation because it fails to consider the effect of body rotation. If the effects of body rotation are averaged into an effective aerodynamic curve, careful analysis of the data indicates that such a curve would be a function of two parameters, α and U.

Two methods were used to analyze experimental data for the square body, providing insight into the evolution of the effective aerodynamic curve with respect to U. Both methods demonstrate the usefulness of employing a surface in $\alpha \times U \times C_N$ space instead of the traditional 2D curve in $\alpha \times C_N$ space.

The trapezoidal body was also considered as an example of geometry less sensitive to curvature effects. It can be seen that the true behavior approaches quasi-steady behavior at high U. Therefore, the model is *conditionally* validated.

Although the quasi-steady assumption fails, the remarkable result is that the overall structure of the aerodynamic model remains intact, permitting the use of aerodynamic force curves, or even surfaces. Considering aerodynamic surfaces opens the door for new methods of optimization. In addition to optimizing the parameters in the harvesting circuit, the natural frequency of the oscillator now presents a method of tuning U for a given V in an environment.

Chapter 5

Geometric Optimization

5.1 Identification of Key Parameters

Due to the experimental complexity of analyzing new bluff geometries, it is useful to assess potential areas of improvement before dedicating significant experimental resources in the investigation of a particular geometry.

To evaluate how the response depends on the aerodynamic coefficients, we can examine a large number of possible system outputs generated by the universal model in Equation 3.54. These outputs were formed using a number of 7^{th}-order, odd aerodynamic polynomials grouped by (i) a constant zero-crossing angle α_0 and (ii) a constant U^*A_1. Recall that the n^{th}-order polynomial coefficient is given by A_n. These collections reduce the nondimensionalized power output to a function of two variables, plotted as a surface in Figure 5.1 for $\alpha_0 = 15.7^\circ$ (matching the classical Parkinson data [68]) and in Figure 5.2 for $\alpha_0 = 20.7^\circ$.

While Figures 5.1 and 5.2 only capture a section of the surface, the visible portion is representative of the trend. It is apparent that, for a fixed α_0 and U^*A_1, there exists an output plateau beyond which no aerodynamic polynomial can improve the response. However, by comparing Figures 5.1 and 5.2, it is apparent that when α_0 is increased and U^*A_1 remains

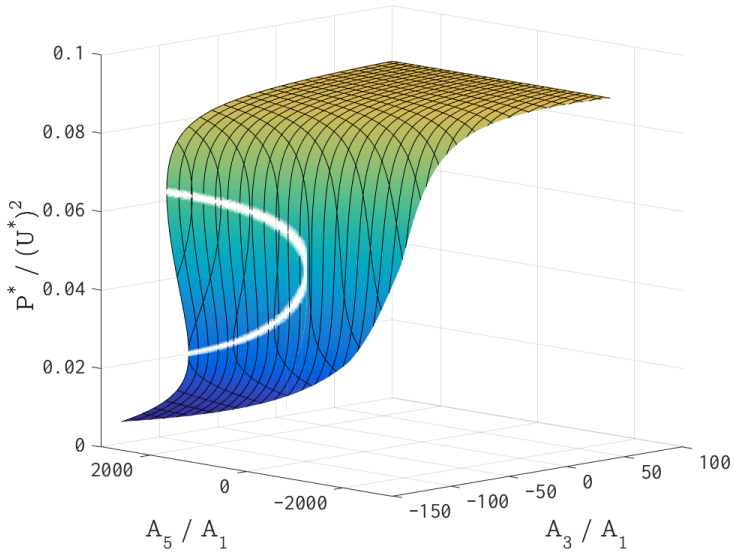

Figure 5.1: Universal response surface for $\alpha_{re} = 15.7°$ and $U^*A_1 = 2$. White streak bounds a fold in the surface.

fixed, there is a significant jump in the plateau magnitude.

The white streak found within the surfaces in Figures 5.1 and 5.2 is representative of a cyclic fold bifurcation (CFB) and bounds an unstable solution region for $P^*/(U^*)^2$. A similar result in the $\hat{\alpha} \times U^*$ space arises in Figure 3.6, wherein a region of instability is bounded by two CFBs. As an example, the Parkinson model oscillator is in this region for $1.25 < U^*A_1 < 1.84$.

Since all the polynomials are scaled by A_1, it is necessary to examine how the output varies with A_1 while α_0 and U^* are fixed. This is most easily accomplished by examining a slice of the $P^*/(U^*)^2$ surface. For convenience, consider the slice containing the set of coefficients corresponding to Parkinson's model, shown in Figure 5.3, where several curves are plotted for multiples of the value provided by Parkinson, *i.e.* $A_1 = 0.5 \cdot 2.69$, $A_1 = 1 \cdot 2.69$, and $A_1 = 2 \cdot 2.69$. The observable trend is that significant changes of A_1 have very little effect on the potential power output, especially for a body such as the square, which is seen to already be near its own plateau; the maximum value of $P^*/(U^*)^2$ only increases by less

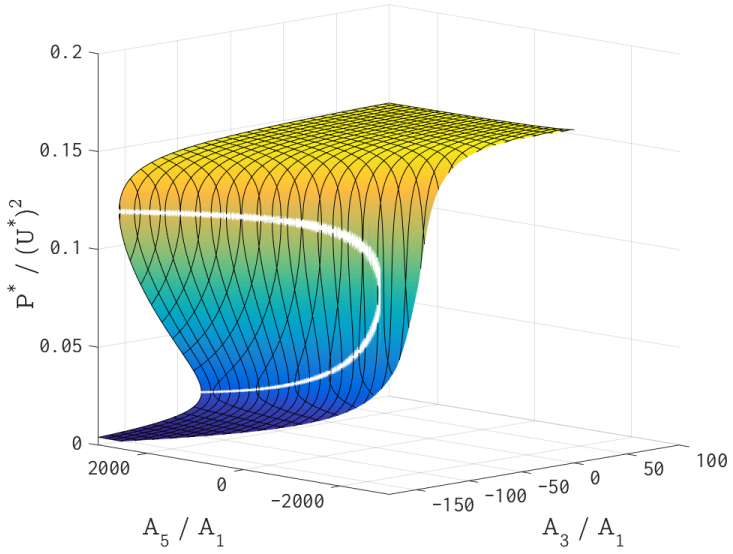

Figure 5.2: Universal response surface for $\alpha_{re} = 20.7°$ and $U^*A_1 = 2$. White streak bounds a fold in the surface.

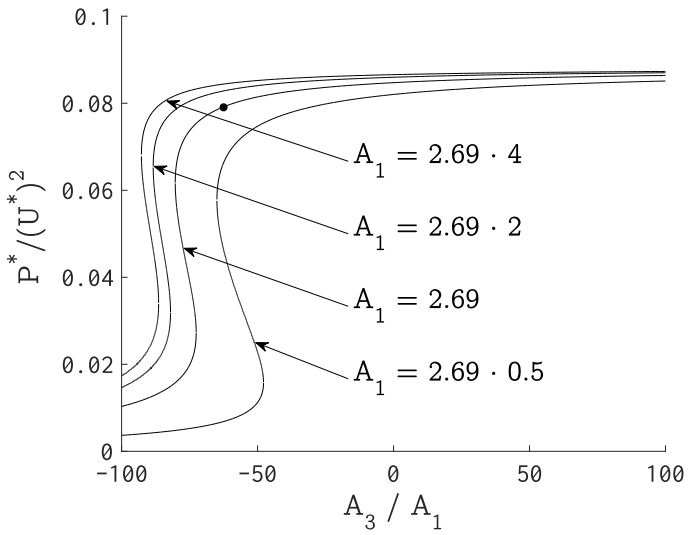

Figure 5.3: A slice of the universal response surface on the plane containing the Parkinson model for the square (black dot). $\alpha_0 = 15.7°$ and $U^* = 1$.

than 1% when A_1 is increased from $A_1 = 0.5 \cdot 2.69$ to $A_1 = 4 \cdot 2.69$. Therefore, we can conclude that the most effective way to increase power output is to focus efforts on increasing α_0. Since α_0 is closely preceded by α_{re}, an increase in the reattachment angle should be accompanied by an increase in the potential output.

5.2 Adjusting the Reattachment Angle

The most straightforward way to increase the reattachment angle is to pull the side faces away from the shear layer, requiring more rotation to bring the side faces into close enough proximity with the shear layers to reattach. The effectiveness of this method is shown in the work of Luo *et al.* [1], who measured the C_N curves for square, trapezoidal, and triangular prisms with the bluff face of width D leading. As the rear face width ranged across D (square), $0.75D$ (trapezoid 1), $0.5D$ (trapezoid 2), and 0 (triangle), the reattachment angles increased from $\alpha_{re} = 12°$, to 20°, to 24°, and to 32°, respectively, as was shown in Figure 2.2.

The disadvantage of tapering the afterbody is that the large distance between the side faces and the shear layers around $\alpha = 0$ inhibits significant interaction between the body and the flow. This is observed in the very small or even negative instability around $\alpha = 0$. Recall that $U^* A_1 = 1$ is a requirement for galloping from rest, and U^* is always positive. Therefore, we see that a body that is unstable over a greater range of α will produce more power only if sufficient stimulus is received. Although the triangular body clearly possesses the greatest potential output, it acts as a "hard" oscillator, and will not begin to self-excite unless provided a sufficient initial condition. Even the trapezoid 1, with a positive A_1, would require a very high cut-in speed of $U^* = 1.7$ (consider the square, which requires $U^* = 0.33$).

An ideal oscillator would combine the at-rest instability of the square profile with the high-amplitude performance of a more tapered geometry. This goal requires side faces both (1) near the flow to promote at-rest instability and (2) far from the flow to allow for

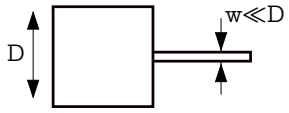

Figure 5.4: Placement of the splitter plate on the body. The width of the plate is small with respect to D.

reattachment at high angles of attack. One feature comes at the cost of the other.

To alleviate the compromise, consider introducing a secondary side surface by extending a splitter plate from the trailing face of the bluff profile, as shown in Figure 5.4. The placement of a streamwise-oriented plate behind the bluff body is not original to this work. Assi [69] found that the addition of a short ($< D$) splitter plate fixed to a circular cylinder amplified galloping response. Although the circular cylinder is not usually prone to gallop due to the lack of asymmetry in its afterbody, the plate extended into the flow field and provided a point of reattachment for the shear layers, allowing the galloping mechanism to be exploited.

To understand how the plate might affect the flow around a square body, consider Bearman's work [70] in which he examined the flow behind a stationary bluff cylinder with splitter plates of varying lengths and observed an increase in shear layer curvature, an influence most pronounced at plate lengths $< 1.5D$. Furthermore, Bearman showed that the addition of a splitter plate behind the body provides for two new interacting shear layers coming off the trailing edges of the square body. The cavity formed between the rear face and the plate traps a secondary recirculation bubble which can aid in lift production. In addition to potentially affecting the lift, the splitter plate was accompanied by a sharp increase in base pressure, reducing drag. Although Bearman did not examine the effect of inducing an angle of attack, the relation between C_{drag} and C_a demonstrates that a reduction in drag at any α will increase the force experienced by the harvester at that angle.

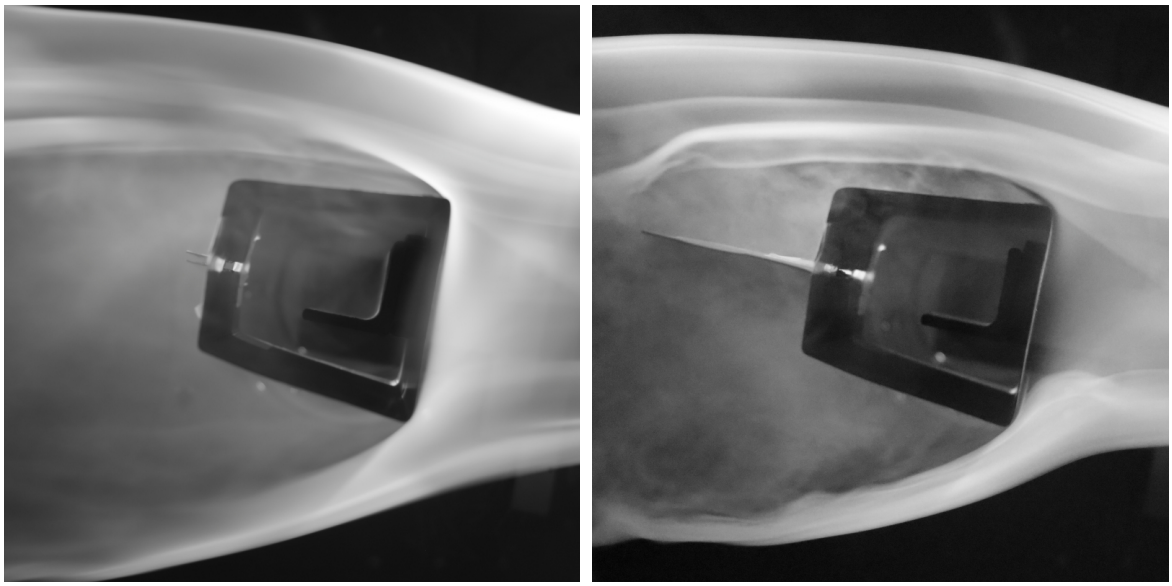

(a) (b)

Figure 5.5: Trapezoid (a) without and (b) with a 4 cm tail at 10° rotation in 2.5 $\mathrm{m\,s^{-1}}$ wind.

5.3 The Addition of a Tail Fin

Fog-based flow visualization tests were run for several profiles in a low-speed wind tunnel environment to note the difference in flow patterns caused by the tail. The clarity of the flow visualization photographs is an area of improvement for future work. Specifically, fog consistency and streamline definition demand attention. However, a few interesting notes can be made. Figure 5.5 allows a side-by-side comparison of a single trapezoidal profile under equivalent conditions with and without a tail fin. Comparing Figures 5.5 (a) and 5.5 (b) shows that the boundary layer over the upper face of the body hugs more closely to the face on the body with a tail. Furthermore, one can observe the increased curvature of the shear layer around the end of the tail in Figure 5.5 (b). This curvature seems to indicate a lower pressure on the upper face of the body, potentially due to a lowered base pressure on the downwind face of the body. These observations would tend to confirm that adding the tail fin permits a higher net lift at the same angle of attack.

The results of increasing the angle of attack to 15° are shown in Figure 5.6. Although

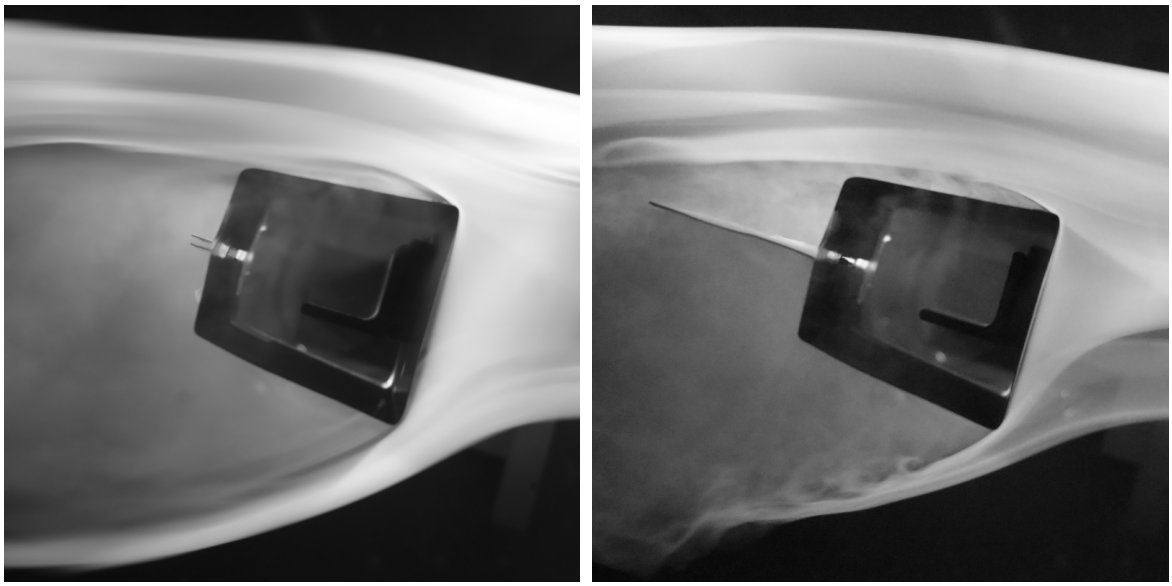

(a) (b)

Figure 5.6: Trapezoid (a) without and (b) with a 4 cm tail at 15° rotation in 2.5 $\mathrm{m\,s^{-1}}$ wind.

both the separated regions in Figure 5.6 are smaller than those in Figure 5.5, the body with the tail has a thinner boundary region, indicating greater suction on the upper face. The shape of the upper shear layer also gives a hint as to the flow around the bodies. The shear layer over the body without a tail, as seen in Figure 5.6 (a), has several large ripples or undulations as it extends from the trailing edge of the top face to the leftmost edge of the photograph. These ripples would tend to indicate strong disturbances in the wake, a typical feature of bluff body wakes. However, Figure 5.6 shows a smooth shear layer extending from the leading edge of the body to the very tip of the tail. This continuity would tend to indicate that the flow above the tail is trapped and does not disturb the shear layer in the same way as a wake would. As a trapped recirculation bubble is a region of low pressure, the tail appears to increase the suction on the upper faces of the body.

5.4 Experimental Investigation

The steady-state amplitude was recorded for a variety of plate lengths affixed to the square and trapezoidal bodies mounted on Beam 1. Small fluctuations in tip mass did not significantly vary the natural frequency; each system was exposed to approximately the same range of U to keep rotational effects consistent. The results for the square body are presented in Figure 5.7.

The results for a body without a tail and a body with a tail of length $0.25D$ are very similar. As the tail length increases to $0.5D$, however, the steady state $\hat{\alpha}$ value further increases for higher values of U^*. The maximum value of $\hat{\alpha}$ is achieved by the body with a $1D$ length tail.

Perhaps more interesting than the maximum $\hat{\alpha}$ value is the monotonic decrease in performance at lower values of U^* as tail length increased. At first glance, this decrease may be due to the effects of body rotation on the galloping mechanism. Further work may repeat the analysis of Section 4.2 for bodies with various tail lengths to evaluate the effect of body rotation as it pertains to tail length.

A similar trend is observed in the results for the trapezoidal body, shown in Figure 5.8. The maximum $\hat{\alpha}$ increases with tail length up to a certain point, in this case $0.4D$ tail length, after which the maximum $\hat{\alpha}$ decreases with increasing tail length.

Also similar is the monotonic decrease in performance at lower U^* with increasing tail length. As discussed previously, the trapezoid is naturally less sensitive than the square to flow curvature. Therefore, the similarity between the square and trapezoidal results may tend to indicate an underlying phenomena independent from body rotation.

For most design implementations, the system parameters may be selected so that the harvester will generally operate in a target range of U^*. Therefore, an "optimum" length may be selected for the desired target range.

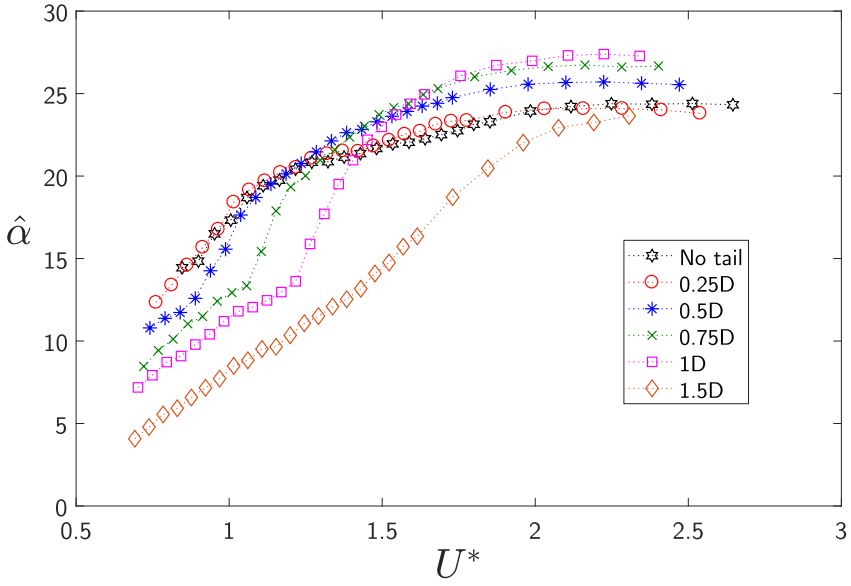

Figure 5.7: Steady state amplitude for the square body.

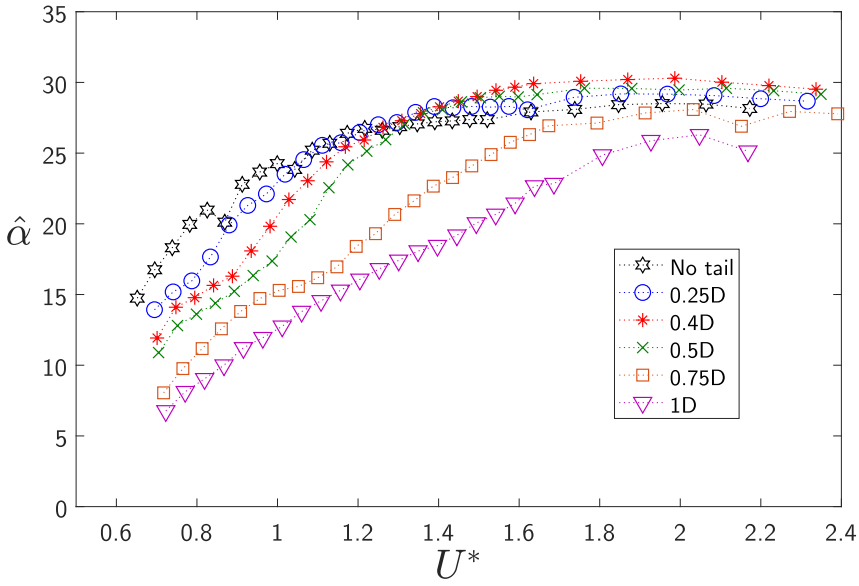

Figure 5.8: Steady state amplitude for the trapezoidal body.

Although there is some trade-off in the maximum amplitude, the "optimum" plate length for the square appears to be the $0.75D$ plate length. The dramatic decrease in performance between $1D$ and $1.5D$ tail lengths is in good agreement with Bearman's observation that the continuous shear layer that provides suction over the top of the body breaks down when the tail length $> 1D$.

The results for the trapezoid in Figure 5.8 show a preference for shorter plate lengths. Furthermore, the boost in amplitude is not as large as for the square, owing to the already advantageous profile of the tapered afterbody. Depending on the target environment, it appears as if the "optimum" plate length is about $0.4D$.

Further experimental trials were run to explore the effects of the plate on output power. The following experiments were conducted using different bodies and beams than previously used. Three bluff profiles were examined: a square, trapezoid ($0.75D$ trailing face), and a triangle (bluff face to vertex length: D, similar to Luo's experiments). all with characteristic cross-stream width $D = 5\,\text{cm}$ and height $10\,\text{cm}$. Each body was mounted on a mild steel beam with length $21.5\,\text{cm}$, width $3\,\text{cm}$, and thickness $0.635\,\text{mm}$. Each profile was tested with no plate, a $2\,\text{cm}$ plate, and a $4\,\text{cm}$ plate. The plate was fixed to the base of the bluff body at the point of attachment to the beam. The plates were notched to avoid interference or any stiffening effects between the beam and the plate. The natural frequency of all systems were equalized before each trial.

A Smart Materials M8528 P2 Macro Fiber Composite strip was glued to the side of the beam to serve as a voltage generator, and a $R = 593\,\text{k}\Omega$ load resistance was connected. The voltage output was divided and measured by a National Instruments MyDAQ ported through a MATLAB Butterworth filter.

The results are presented in Figure 5.9. Two tail lengths for both bodies are included to establish corroboration with the results from the previously discussed experiment. At first look, the agreement is remarkable: (1) the top performer is the trapezoid with a $0.4D$ tail,

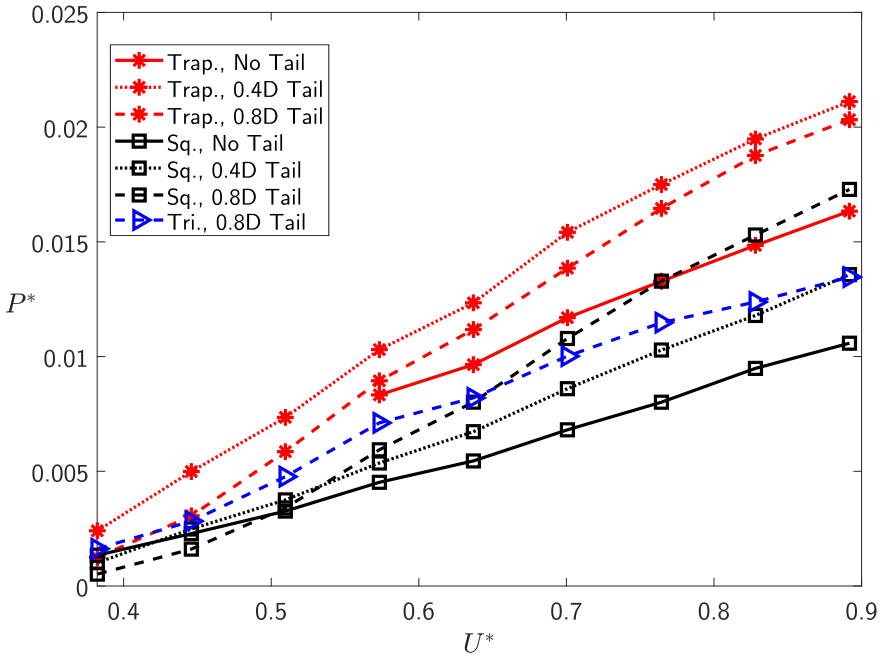

Figure 5.9: The nondimensional output power generated experimentally.

(2) the best performing square combination uses the $0.8D$ tail, and (3) the square with a $0.4D$ tail performed worse than that with a $0.8D$ tail but better than the square with no tail.

However, some results were unexpected. The measured response of the trapezoid with the $0.8D$ tail is in disagreement with the results shown in Figure 5.8. Furthermore, the triangle, being a hard oscillator, did not gallop from rest without a tail and did not demonstrate steady-state galloping with the $0.4D$ tail, but with the $0.8D$ tail, the body had enough instability to gallop from rest.

For both the square and the trapezoid, the addition of the tail fin allowed a significant optimization of the output power. The trapezoid with $0.4D$ and $0.8D$ tails, respectively, experienced a maximum 28% and 24% improvement in output power, while the square with the same tails experienced a maximum 27% and 60% improvement, respectively. The straight sides of the square body are relatively limiting with respect to the reattachment angle, so it is reasonable that it experiences the greatest percent improvement.

Chapter 6

Conclusions and Future Work

The first objective of this work was to identify the physical mechanisms at work when a galloping body is exposed to finite tip rotation. To this end, a review of bluff body aerodynamics identified some known fluid mechanisms which operate on rotating bodies. It was shown in Chapter 2 that the quasi-steady theory, which has traditionally been applied to model galloping behavior, is insufficient to describe the aerodynamics around a galloping body in the presence of finite tip rotation. The flow curvature induced by the rotating body has profound effects on the lift and drag experienced by the body.

To help understand how a GFEH with tip rotation deviates from behavior predicted by the quasi-steady theory, the traditional dynamical model was adapted in Chapter 3 to include the kinematic effects of tip rotation. After the traditional linearized Euler-Bernoulli beam model was compared with a large-displacement formulation to test the limits of the small angle assumption, it was found that a linear displacement-to-rotation ratio can accurately predict the rotation of the tip of a cantilever beam over a useful range of displacement amplitude. This linear relationship was employed to develop a closed-form approximate analytical solution to the GFEH response. After developing the solution, it was shown that neglecting the tip rotation will always over-predict the output power of a GFEH, highlighting

the importance of its inclusion in future work.

The approximate analytical solution was employed to infer the effect of tip rotation on the effective aerodynamic forces on the GFEH system based on a number of experimental trials in Chapter 4. Although the quasi-steady assumption fails, the remarkable result is that the overall structure of the aerodynamic model remains intact. The analysis suggests the existence of a unifying theory sufficient to modify existing aerodynamic force descriptions to be functions of some tip rotation factor. The aerodynamic model adopted by the present work to account for tip rotation demonstrated potential improvement over the quasi-steady model but further work is required to refine the necessary optimization algorithms.

The second objective sought to optimize the power output of GFEH using geometric modifications inspired by an understanding of the underlying physics. The quasi-steady model employed for GFEH design indicated that the critical limiting factor for steady-state power production is the angle of attack at which flow reattaches to the bluff body. Relevant literature on bluff body aerodynamics suggested that a splitter plate extending from the trailing face of the bluff body can be used to alter the flow over the body. Therefore, a GFEH was proposed in Chapter 5 that employs a splitter plate as a tail fin to adjust the reattachment angle of attack.

The performance enhancement was clear in experimental trials. Furthermore, using a tail fin on some bluff profiles, such as the triangle, can increase the useful range of galloping instability for energy harvesting. Initial experimental trials indicate that an optimized oscillator benefits from both a tapered main body and an attached splitter plate, as the best performer was an augmented trapezoid. Significant work remains to ascertain the optimum configuration and how the "optimum" may vary for different environmental considerations.

References

[1] S.C. Luo, M.G. Yazdani, Y.T. Chew, and T.S. Lee. Effects of incidence and afterbody shape on flow past bluff cylinders. *Journal of wind engineering and industrial aerodynamics*, 53(3):375–399, 1994.

[2] C Norberg. Flow around rectangular cylinders: pressure forces and wake frequencies. *Journal of wind engineering and industrial aerodynamics*, 49(1-3):187–196, 1993.

[3] G Alonso. *Fenomenos de galope en obstaculos de section no rectangular*. PhD thesis, Ph. D. Thesis, Universidad Politecnica de Madrid, 2005.

[4] Lawrence W. Carr, Kenneth W. McAlister, and William J. McCroskey. Analysis of the development of dynamic stall based on oscillating experiments. Technical Report TN D-8382, National Aeronautics and Space Administration, Washington, USA, January 1977. Prepared in cooperation with Army Air Mobility Lab, Moffett Field, CA.

[5] Arnold M. Kuethe and Chuen-Yen Chow. *Foundations of Aerodynamics: Bases of Aerodynamic Design*. John Wiley & Sons, Inc., 5 edition, 1998.

[6] Vijay Raghunathan, Curt Schurders, Sung Park, and Mani B. Srivastava. Energy-aware wireless microsensor networks. *IEEE Signal Processing Magazine*, 19(2):40–50, 2002.

[7] Christian C. Enz, Amre El-Hoiydi, Jean-Dominique Decotignie, and Vincent Peiris. Wisenet: An ultralow-power wireless sensor network solution. *Computer*, 37(8):62–70, 2004.

[8] Shad Roundy, Brian P. Otis, Yuen-Hui Chee, Jan M. Rabaey, and Paul Wright. A 1.9 GHz rf transmit beacon using environmentally scavenged energy. Technical report, Department of Mechanical Engineering, University of California, Berkeley, 2003.

[9] Philippe Giguère and Michael S. Selig. Low reynolds number airfoils for small horizontal axis wind turbines. *Wind Engineering*, 21(6), 1997.

[10] Geoffrey Parkinson. Phenomena and modelling of flow-induced vibrations of bluff bodies. *Progress in Aerospace Sciences*, 26(2):169–224, 1989.

[11] Z.C. Yang and L.C. Zhao. Analysis of limit cycle flutter of an airfoil in incompressible flow. *Journal of Sound and Vibration*, 123(1):1 – 13, 1988.

[12] C.H.K. Williamson, , and R. Govardhan. Vortex-induced vibrations. *Annual Review of Fluid Mechanics*, 36(1):413–455, 2004.

[13] Robert D. Blevins. *Flow-induced vibration*. Van Nostrand Reinhold Co., New York, NY, 2nd edition, 1990.

[14] Matthew Bryant and Ephrahim Garcia. Modeling and testing of a novel aeroelastic flutter energy harvester. *Journal of Vibration and Acoustics*, 133:011010–1– 011010–11, 2011.

[15] Amin S. Bibo. *Investigation of Concurrent Energy Harvesting from Ambient Vibrations and Wind*. PhD thesis, Clemson University, August 2014.

[16] Carlos De Marqui and Alper Erturk. Electroaeroelastic analysis of airfoil-based wind energy harvesting using piezoelectric transduction and electromagnetic induction. *Journal of Intelligent Material Systems and Structures*, 2012.

[17] Fei Fei, John D. Mai, and Wen Jung Li. A wind-flutter energy converter for powering wireless sensors. *Sensors and Actuators A: Physical*, 173(1):163 – 171, 2012.

[18] Huseyin Dogus Akaydin, Niell Elvin, and Yiannis Andreopoulos. Energy harvesting from highly unsteady fluid flows using piezoelectric materials. *Journal of Intelligent Material Systems and Structures*, 21(13):1263–1278, 2010.

[19] A. Mehmood, A. Abdelkefi, M.R. Hajj, A.H. Nayfeh, I. Akhtar, and A.O. Nuhait. Piezoelectric energy harvesting from vortex-induced vibrations of circular cylinder. *Journal of Sound and Vibration*, 332(19):4656 – 4667, 2013.

[20] J.P. Den Hartog. *Mechanical vibrations*. Courier Corporation, 1985.

[21] G.V. Parkinson and J.D. Smith. The square prism as an aeroelastic non-linear oscillator. *The Quarterly Journal of Mechanics and Applied Mathematics*, 17(2):225–239, 1964.

[22] Y. Nakamura and Y. Tomonari. Galloping of rectangular prisms in a smooth and in a turbulent flow. *Journal of Sound and Vibration*, 52(2):233–241, 1977.

[23] Y. Nakamura, K. Hirata, and T. Urabe. Galloping of rectangular cylinders in the presence of a splitter plate. *Journal of Fluids and Structures*, 5(5):521 – 549, 1991.

[24] AN Ryabinin and VD Lyusin. Galloping of small aspect ratio square cylinder. *ARPN Journal of Engineering and Applied Sciences*, 10(1):134–138, 2015.

[25] Felix Ewere and Gang Wang. Performance of galloping piezoelectric energy harvesters. *Journal of Intelligent Material Systems and Structures*, 25(14):1693–1704, 2013.

[26] Robert D. Blevins. *Flow-induced vibration.* Van Nostrand Reinhold Co., New York, NY, 1977.

[27] Robert D. Blevins. *Flow Induced Vibrations of Bluff Structures.* PhD thesis, California Institute of Technology, 1974.

[28] Y Nakamura. On the aerodynamic mechanism of torsional flutter of bluff structures. *Journal of Sound and Vibration*, 67(2):163–177, 1979.

[29] Masaru Matsumoto. Aerodynamic damping of prisms. *Journal of Wind Engineering and Industrial Aerodynamics*, 59(2-3):159–175, 1996.

[30] Michael P. Païdoussis, Stuart J. Price, and Emmanuel De Langre. *Fluid-structure interactions: cross-flow-induced instabilities.* Cambridge University Press, 2010.

[31] Y.C. Fung. *An Introduction to the Theory of Elasticity.* John Wiley & Sons, 1955.

[32] P.W. Bearman, I.S. Gartshore, D.J. Maull, and G.V. Parkinson. Experiments on flow-induced vibration of a square-section cylinder. *Journal of Fluids and Structures*, 1(1):19 – 34, 1987.

[33] SC Luo, YT Chew, and YT Ng. Hysteresis phenomenon in the galloping oscillation of a square cylinder. *Journal of Fluids and Structures*, 18(1):103–118, 2003.

[34] Mario Lee and Chih-Ming Ho. Lift force of delta wings. *Applied Mechanics Reviews*, 43(9):209–221, 1990.

[35] M. I. Kazakevich and A.G. Vasilenko. Closed analytical solution for galloping aeroelastic self-oscillations. *Journal of Wind Engineering and Industrial Aerodynamics*, 65:353–360, 1996.

[36] Y. Nakamura. On the aerodynamic mechanism of torsional flutter of bluff structures. *Journal of Sound and Vibration*, 67(2):163 – 177, 1979.

[37] BW Van Oudheusden. Rotational one-degree-of-freedom galloping in the presence of viscous and frictional damping. *Journal of fluids and structures*, 10(7):673–689, 1996.

[38] BW Van Oudheusden. Aerodynamic stiffness and damping effects in the rotational galloping of a rectangular cross-section. *Journal of fluids and structures*, 14(8):1119–1144, 2000.

[39] BW Van Oudheusden. Aerodynamic stiffness effects in rotational galloping at high wind speeds. *Journal of wind engineering and industrial aerodynamics*, 64(1):31–46, 1996.

[40] JM Kluger, FC Moon, and RH Rand. Shape optimization of a blunt body vibro-wind galloping oscillator. *Journal of Fluids and Structures*, 40:185–200, 2013.

[41] Robert H Scanlan. Problematics in formulation of wind-force models for bridge decks. *Journal of Engineering Mechanics*, 119(7):1353–1375, 1993.

[42] William J McCroskey. The phenomenon of dynamic stall. Technical report, NATIONAL AERONUATICS AND SPACE ADMINISTRATION, MOFFETT FIELD, CA. AMES RESEARCH CENTER, 1981.

[43] W MCCROSKEY and S PUCCI. Viscous-inviscid interaction on oscillating airfoils in subsonic flow. In *19th Aerospace Sciences Meeting*, page 51, 1981.

[44] M Kramer. Increase in the maximum lift of an airfoil due to a sudden increase in its effective angle of attack resulting from a gust. *NASA TM-678*, 1932.

[45] Mizuyasu Koide, Yuuki Kubo, Tsutomu Takahashi, László Baranyi, and Masataka Shirakashi. The vibration response of a cantilevered rectangular cylinder in cross-flow oscillation. *Transactions of the ASME-I-Journal of Fluids Engineering*, 126(5):884–887, 2004.

[46] William J McCroskey. Unsteady airfoils. *Annual review of fluid mechanics*, 14(1):285–311, 1982.

[47] M Dickinson. The effects of wing rotation on unsteady aerodynamic performance at low reynolds numbers. *Journal of experimental biology*, 192(1):179–206, 1994.

[48] Michael H Dickinson, Fritz-Olaf Lehmann, and Sanjay P Sane. Wing rotation and the aerodynamic basis of insect flight. *Science*, 284(5422):1954–1960, 1999.

[49] Sanjay P Sane and Michael H Dickinson. The aerodynamic effects of wing rotation and a revised quasi-steady model of flapping flight. *Journal of experimental biology*, 205(8):1087–1096, 2002.

[50] Sanjay P Sane. The aerodynamics of insect flight. *Journal of experimental biology*, 206(23):4191–4208, 2003.

[51] Amin Bibo and Mohammed F Daqaq. An analytical framework for the design and comparative analysis of galloping energy harvesters under quasi-steady aerodynamics. *Smart Materials and Structures*, 24(9):094006, 2015.

[52] A. Abdelkefi, M.R. Hajj, and A.H. Nayfeh. Piezoelectric energy harvesting from transverse galloping of bluff bodies. *Smart Materials and Structures*, 22(1):015014, 2013.

[53] Alper Erturk and Daniel J Inman. *Piezoelectric energy harvesting*. John Wiley & Sons, 2011.

[54] AH Nayfeh and SA Nayfeh. On nonlinear modes of continuous systems. *Journal of Vibration and Acoustics*, 116(1):129–136, 1994.

[55] AH Nayfeh, C Chin, and SA Nayfeh. Nonlinear normal modes of a cantilever beam. *Journal of vibration and acoustics*, 117(4):477–481, 1995.

[56] Hiroshi Yabuno, Yoshiro Ide, and Nobuharu Aoshima. Nonlinear analysis of a parametrically excited cantilever beam: Effect of the tip mass on stationary response (special issue on nonlinear dynamics). *JSME International Journal Series C Mechanical Systems, Machine Elements and Manufacturing*, 41(3):555–562, 1998.

[57] Hsieh Shang-Rou, Steven W Shaw, and Christophe Pierre. Normal modes for large amplitude vibration of a cantilever beam. *International Journal of Solids and Structures*, 31(14):1981–2014, 1994.

[58] Christopher Sugino, David Tan, Stephen Leadenham, and Alper Erturk. Dramatic effect of fluid damping on the performance of a nonlinear m-shaped broadband energy harvester. In *Active and Passive Smart Structures and Integrated Systems 2016*, volume 9799, 2016.

[59] EW Woolam. Drag coefficients for flat square plates oscillating normal to their planes in air. *NASA CR-66544, March*, 1968.

[60] Garbis H. Keulegan and Lloyd H. Carpenter. Forces on cylinders and plates in an oscillating fluid. *Journal of Research of the National Bureau of Standards*, 60(5):423–440, 1958.

[61] Wilfred E. Baker, William E. Woolam, and Dana Young. Air and internal damping of thin cantilever beams. *International Journal of Mechanical Sciences*, 9(11):743 – 766, 1967.

[62] A. Barrero-Gil, G. Alonso, and A. Sanz-Andres. Energy harvesting from transverse galloping. *Journal of Sound and Vibration*, 329(14):2873 – 2883, 2010.

[63] Milos Novak. Aeroelastic galloping of prismatic bodies. *Journal of the Engineering Mechanics Division*, 95(1):115–142, 1969.

[64] Sergei L Shmakov. A universal method of solving quartic equations. *International Journal of Pure and Applied Mathematics*, 71(2):251–259, 2011.

[65] G. Alonso, Alfredo Sanz-Lobera, and J. Meseguer. Hysteresis phenomena in transverse galloping of triangular cross-section bodies. *Journal of Fluids and Structures*, 33:243–251, 2012.

[66] Antonio Barrero-Gil, A Sanz-Andrés, and G Alonso. Hysteresis in transverse galloping: the role of the inflection points. *Journal of Fluids and Structures*, 25(6):1007–1020, 2009.

[67] Kenneth Price, Rainer M Storn, and Jouni A Lampinen. *Differential evolution: a practical approach to global optimization*. Springer Science & Business Media, 2006.

[68] Mitchell A Wawzonek. *Aeroelastic behavior of square section prisms in uniform flow*. PhD thesis, University of British Columbia, 1979.

[69] Gustavo RS Assi and Peter W Bearman. Transverse galloping of circular cylinders fitted with solid and slotted splitter plates. *Journal of Fluids and Structures*, 54:263–280, 2015.

[70] PW Bearman. Investigation of the flow behind a two-dimensional model with a blunt trailing edge and fitted with splitter plates. *Journal of Fluid Mechanics*, 21(02):241–255, 1965.

Appendices

Appendix A

Parallax Correction

Let Δm denote the measured value from the vibrometer as shown in Figure A.1. For square bodies, $w = \frac{1}{2}D$. For trapezoidal bodies, $w = \tan^{-1}\left(\frac{1-r}{2}\right)$ where r is the ratio of front to back face width (i.e., for $r = 0.75$ the rear face is $0.75D$). The true ΔY can be calculated as

$$\Delta Y = \Delta m - w + w\cos\theta - (\Delta X - w\sin\theta)\tan(\theta - \phi)\,. \tag{A.1}$$

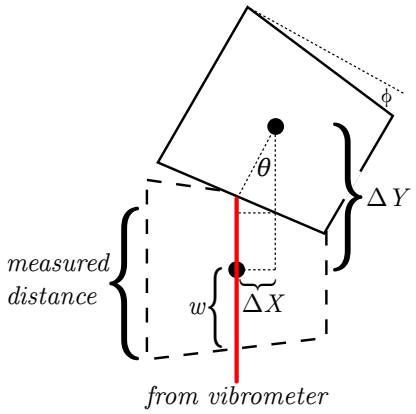

Figure A.1: Diagram for the method of parallax correction.

Appendix B

ANSYS APDL Code for Beam Simulation

```
/PREP7
*SET,WIDTH,0.0025
*SET,HEIGHT,0.015
*SET,LENGTH,0.3
*SET,TIPMASS,0.15
*SET,TIPINERTIA,5e-6
*SET,TIPWIDTH,SQRT((TIPINERTIA - TIPMASS*0.005**2)/(1/12*TIPMASS) - 0.005**2)
*SET,FORCING,4*9.81
*SET,NODENUM,32 ! MAKE SURE OUTPUT FILE FORMAT MATCHES
*SET,EVALTIME,10

/UNITS,MKS

!*** SET MATERIAL PROPERTIES
! FOR THE BEAM
MPTEMP,1,0
MPDATA,EX,1,,70e9
MPDATA,PRXY,1,,.3
MPDATA,DENS,1,,2700
! FOR THE TIP BODY
```

```
MPDATA,EX,2,,200e9
MPDATA,PRXY,2,,.3
MPDATA,DENS,2,,TIPMASS/(0.005*TIPWIDTH*HEIGHT)

!*** SET BEAM GEOMETRY
SECTYPE,   1, BEAM, RECT, , 0
SECOFFSET, CENT
SECDATA,WIDTH,HEIGHT,0,0,0,0,0,0,0,0,0,0
SECTYPE,   2, BEAM, RECT, , 0
SECOFFSET, CENT
SECDATA,TIPWIDTH,HEIGHT,0,0,0,0,0,0,0,0,0,0

!*** DEFINE MESH
! DEFINE NODES
N,1,0,0,0
N,NODENUM-1,LENGTH,0,0
FILL,1,NODENUM-1
N,NODENUM,LENGTH+0.005,0,0
! FIX ONE END
D,ALL,UZ,0,,,,ROTX,ROTY
D,1,ALL
! DEFINE ELEMENT TYPE
ET,1,BEAM188
! DEFINE ELEMENTS FOR BEAM
TYPE,1
MAT,1
REAL,
ESYS,0
SECNUM,1
TSHAP,LINE
E,1,2
EGEN,NODENUM-2,1,-1
! DEFINE ELEMENT FOR TIP BODY
TYPE,1
MAT,2
REAL,
ESYS,0
```

```
SECNUM,2
TSHAP,LINE
E,NODENUM-1,NODENUM

!*** SOLVE FOR FIRST MODAL FREQUENCY
/SOL
ANTYPE,2
MODOPT,SUBSP,5
MXPAND,5, , ,0
LUMPM,0
PSTRES,0
MODOPT,SUBSP,5,0,0, ,OFF
RIGID,
SUBOPT,STRMCHK,0
SUBOPT,MEMORY,AUTO
SOLVE
FINISH
/POST1
! SET FORCING FREQUENCY TO NATURAL FREQUENCY
*GET,FORCING_FREQ,MODE,1,FREQ

! ENTER SOLUTION MODE
/SOL

! DEFINE ACCELERATION INPUT
*DEL,_FNCNAME
*DEL,_FNCMTID
*DEL,_FNC_C1
*DEL,_FNC_C2
*DEL,_FNCCSYS
*SET,_FNCNAME,'shaker'
*DIM,_FNC_C1,,1
*DIM,_FNC_C2,,1
*SET,_FNC_C1(1),FORCING
*SET,_FNC_C2(1),FORCING_FREQ
*SET,_FNCCSYS,0
*DIM,%_FNCNAME%,TABLE,6,4,1,,,,%_FNCCSYS%
```

```
! Begin of equation: FORCING*sin(FORCING_FREQ*{TIME})
*SET,%_FNCNAME%(0,0,1), 0.0, -999
*SET,%_FNCNAME%(2,0,1), 0.0
*SET,%_FNCNAME%(3,0,1), %_FNC_C1(1)%
*SET,%_FNCNAME%(4,0,1), %_FNC_C2(1)%
*SET,%_FNCNAME%(5,0,1), 0.0
*SET,%_FNCNAME%(6,0,1), 0.0
*SET,%_FNCNAME%(0,1,1), 1.0, -1, 0, 1, 18, 3, 1
*SET,%_FNCNAME%(0,2,1), 0.0, -1, 9, 1, -1, 0, 0
*SET,%_FNCNAME%(0,3,1),   0, -2, 0, 1, 17, 3, -1
*SET,%_FNCNAME%(0,4,1), 0.0, 99, 0, 1, -2, 0, 0
! End of equation: FORCING*sin(FORCING_FREQ*{TIME})
ACEL,,%shaker%,

! SET UP NONLINEAR TRANSIENT SIMULATION
ANTYPE,4
TRNOPT,FULL
LUMPM,0
NLGEOM,1
DELTIM,0.00075,0.000001,0.001
OUTRES,ERASE
OUTRES,NSOL,ALL
BETAD,0.001
TIME,EVALTIME
SOLVE

!*** SAVE DATA IN .TXT FILE
/POST26
! ALLOCATE VARIABLE STORAGE
NUMVAR,200
! SET VARIABLE NAMES FOR ALL NODAL DISPLACEMENT SOLUTIONS
*DO,loop_counter,2,NODENUM,1
NSOL,loop_counter,loop_counter,U,Y
NSOL,loop_counter+NODENUM,loop_counter,U,X
*ENDDO
! STORE VARIABLES
STORE,MERGE
```

```
132 ! DETERMINE SIZE OF SOLUTION ARRAYS
133 *GET,size,VARI,,NSETS
134 ! ALLOCATE ARRAYS
135 *dim,UYMAT,array,size,NODENUM
136 *dim,UXMAT,array,size,NODENUM
137 ! FILL FIRST COLUMN WITH TIME VECTOR
138 VGET,UYMAT(1,1),1
139 VGET,UXMAT(1,1),1
140 ! FILL SUBSEQUENT COLUMNS OF UYMAT WITH DISPLACEMENT IN Y
141 *DO,loop_counter,2,NODENUM,1
142 VGET,UYMAT(1,loop_counter),loop_counter
143 *ENDDO
144 ! FILL SUBSEQUENT COLUMNS OF UXMAT WITH DISPLACEMENT IN X
145 *DO,loop_counter,2,NODENUM,1
146 VGET,UXMAT(1,loop_counter),loop_counter+NODENUM
147 *ENDDO
148 ! WRITE TO FILE
149 *MWRITE,UYMAT(1,1),displacement_y,txt,,,NODENUM,NSETS,1
150 (31((f)',')(f))
151 *MWRITE,UXMAT(1,1),displacement_x,txt,,,NODENUM,NSETS,1
152 (31((f)',')(f))
153
154 /EOF
```

Appendix C

Uncertainty in U^*

The experimental results rely heavily on the correct identification of the mechanical damping ratio ζ_m. If overestimated, the results will suggest that the system experiences a large aerodynamic force to overcome an artificially inflated mechanical dissipative element. If underestimated, the results will similarly underpredict the amount of work input by the fluid flow.

To appreciate the sensitivity of the experimental interpretation, consider an uncertainty propagation analysis of U^*, a critical parameter in the approximate analytical solution (Equation 3.54). The total uncertainty is equal to the root-sum-of-squares of the zeroth order uncertainty contributions of all the component measurements: D,H,V,ρ_a, ζ_m, ω, and M_{eff}.

$$U^* = \frac{\rho_a V D H}{4\zeta_m \omega M_{eff}} \tag{C.1}$$

$$\begin{aligned} u_{U^*} = \Bigg[&\left(\frac{\partial U^*}{\partial D} u_D\right)^2 + \left(\frac{\partial U^*}{\partial H} u_H\right)^2 + \left(\frac{\partial U^*}{\partial V} u_V\right)^2 + \left(\frac{\partial U^*}{\partial \rho_a} u_{\rho_a}\right)^2 \\ &+ \left(\frac{\partial U^*}{\partial \zeta_m} u_{\zeta_m}\right)^2 + \left(\frac{\partial U^*}{\partial \omega} u_\omega\right)^2 + \left(\frac{\partial U^*}{\partial M_{eff}} u_{M_{eff}}\right)^2 \Bigg]^{0.5} \end{aligned} \tag{C.2}$$

The length scales were measured with $u_D = u_H = 0.001\,\mathrm{m}$. The anemometer allowed

$u_V = 0.05\,{}^{\mathrm{m}}/_{\mathrm{s}}$. The density of air is given an uncertainty of $u_{\rho_a} = 0.05\rho_a$ to accommodate fluctuation in humidity and temperature. Because the measurement of frequency is subject predominantly to the sampling rate at 1000 Hz, $u_\omega \approx 0$.

By far the most volatile component is ζ_m. If the purely linear mechanical damping interpretation employed by this study is accurate, the only uncertainty in ζ_m can be found by expanding the linear regression equations to give the uncertainty in terms of the displacement measurements and the corresponding uncertainty of $u_y = 40\,\mu\mathrm{m}$ as

$$u_{\zeta_m} = \sqrt{\sum_{j=1}^{N}\left(\frac{\partial \zeta_m}{\partial y'_j}u_y\right)^2 + \sum_{j=1}^{N}\left(\frac{\partial \zeta_m}{\partial y_j}u_y\right)^2} \tag{C.3}$$

where

$$\frac{\partial \zeta_m}{\partial y'_j} = \frac{\sum_{k=1}^{N} y_k^3 y_j^2 - \sum_{k=1}^{N} y_k^4 y_j}{\sum_{k=1}^{N} y_k^2 \sum_{k=1}^{N} y_k^4 - \left(\sum_{k=1}^{N} y_k^3\right)^2} \tag{C.4}$$

and

$$\frac{\partial \zeta_m}{\partial y_j} = \frac{\sum_{k=1}^{N} y_k^3 y_j^2 - \sum_{k=1}^{N} y_k^4 y_j}{\sum_{k=1}^{N} y_k^2 \sum_{k=1}^{N} y_k^4 - \left(\sum_{k=1}^{N} y_k^3\right)^2} \tag{C.5}$$

With high sampling rates over an extended period of time (high N), the uncertainty introduced by the linear regression is negligible. However, the preceding uncertainty analysis for ζ_m only evaluates the uncertainty introduced by the regression and not the uncertainty introduced by presuming purely linear mechanical damping. To visualize how a small error in discerning the true value of the mechanical damping propagates into uncertainty in U^*, Figure C.1 presents the total uncertainty in U^* as a function of both the true value of ζ_m and the uncertainty of that value. It is apparent that even a slight misinterpretation of the damping model drastically disrupts the uncertainty of U^*. Given the critical role of the parameter U^*, properly determining the mechanical damping ratio is paramount to accurate interpretation of the experimental results.

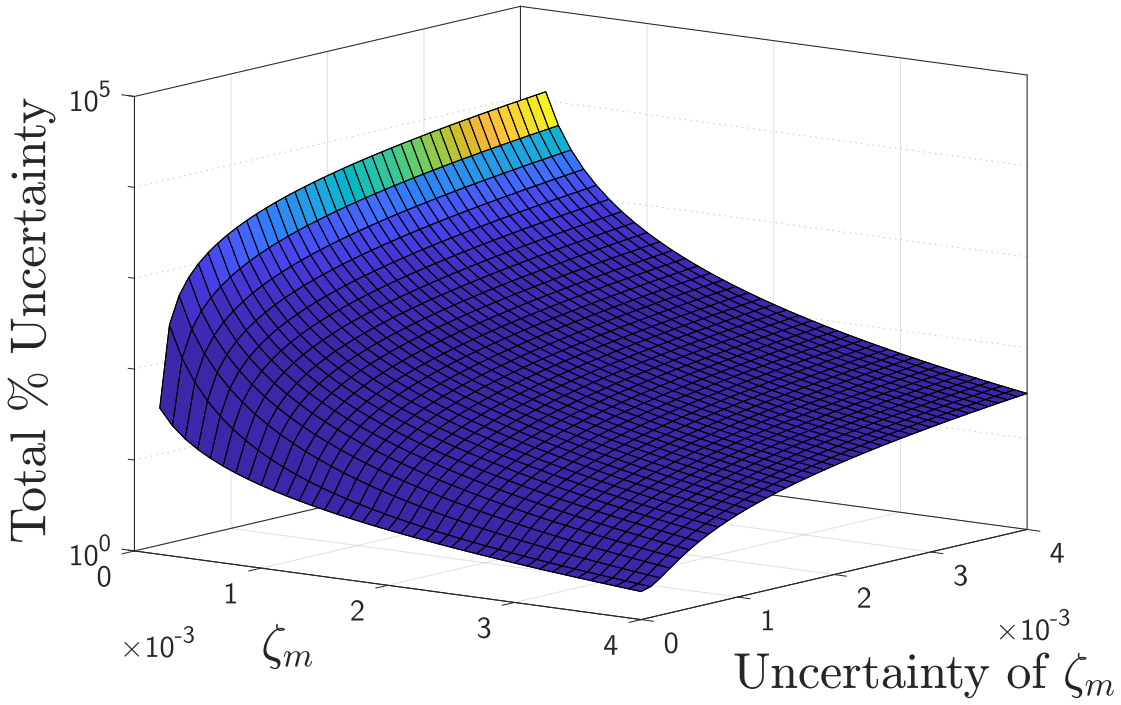

Figure C.1: The uncertainty in U^* as it relates to the true value of ζ_m and any uncertainty thereof.